Title

Wirelessly Powered Localization Systems for Biomedical and Environmental Applications

Author

Ray, Arkaprova

Publication Date

2024

Peer reviewed|Thesis/dissertation

UNIVERSITY OF CALIFORNIA

Los Angeles

Wirelessly Powered Localization Systems for Biomedical and Environmental Applications

A thesis submitted in partial satisfaction

of the requirements for the degree

Master of Science in Electrical and Computer Engineering

by

Arkaprova Ray

2024

ABSTRACT OF THE THESIS

Wirelessly Powered Localization Systems for Biomedical and Environmental Applications

by

Arkaprova Ray
Master of Science in Electrical and Computer Engineering
University of California, Los Angeles, 2024
Professor Aydin Babakhani, Chair

The recent emergence of the Internet of Things (IoT) has coincided with the popularity of wireless sensor networks (WSNs), which transmit and receive data to and from IoT devices. Wirelessly powered WSNs offer significant advantages over battery-powered WSNs since they do not suffer from issues regarding battery leakage and limited battery life.

This thesis presents two miniaturized wireless and battery-less localization systems for use in WSNs. Both systems comprise a printed circuit board (PCB) having a microchip, on-PCB coils, and resonating capacitors. The microchip, fabricated in the TSMC 180 nm process, is wirelessly powered by an RF signal and transmits back a locked sub-harmonic signal generated from the powering signal, eliminating the need for a power-hungry oscillator. The PCB has a form factor of 17 mm $\times$ 12 mm $\times$ 0.2 mm. The first system, having a 6 µW power consumption, has been proposed to be used for wireless capsule endoscopy and demonstrates an accuracy of less than 5 mm in ex vivo measurements. Additionally, the system has been verified to detect a motion as small as 50 µm, as well as rates of motion up to 10 bpm. The second system, having a 1.5 µW power consumption, has been proposed to be used for fracture mapping at temperatures up to 250 °C and pressures up to 24 MPa.

The thesis of Arkaprova Ray is approved.

Behzad Razavi

Yuanxun Wang

Aydin Babakhani, Committee Chair

University of California, Los Angeles

2024

To my parents . . .

TABLE OF CONTENTS

LIST OF FIGURES

LIST OF TABLES

ACKNOWLEDGMENTS

I want to thank my advisor Prof. Aydin Babakhani, for giving me the opportunity to work on many interesting projects and providing guidance, valuable feedback, and support throughout my time at UCLA. I am also grateful to Prof. Behzad Razavi and Prof. Y. Ethan Wang for graciously agreeing to be a part of my thesis committee.

I thank Prof. Behzad Razavi, Prof. Asad Abidi, and Prof. Sudhakar Pamarti for their brilliant courses at UCLA, which have greatly helped me strengthen my foundation in analog/mixed-signal and RF circuit design. I would also like to thank Prof. Mrigank Sharad, Prof. Pradip Mandal, and Prof. Bibhu Datta Sahoo for their courses during my undergrad at IIT Kharagpur, which sparked my interest in circuit design.

I want to thank my colleagues and labmates Sidharth, Iman, Jaskirat, Roshan, Benyamin, Hamid, Wei, Jaeeun, Sam, and Mostafa at the Integrated Sensors Lab (ISL) at UCLA, for being always extremely helpful and supportive, as well as making the lab a fun place to work. I will fondly remember the discussions on a broad spectrum of topics that I have had with you. Additionally, I would like to thank Utkarsh, Kshitij, Vinod, Pawan, Chandrakanth, Saranyu, and Joshua for their advice on different matters.

Finally, I thank my parents for their unwavering love and support.

VITA

2015-2020 B.Tech., Electronics and Communication Engineering, Indian Institute of Technology Kharagpur, India

2020-2024 Research Assistant, Electrical and Computer Engineering, University of California, Los Angeles, USA

CHAPTER 1

Introduction

With the advent of the Internet of Things (IoT), wireless sensor networks (WSN) are becoming increasingly popular in recent years for use in various applications [1–3]. These networks include many spatially scattered sensor nodes, each of which senses some information from its environment, processes it, and transmits the processed data back to another node or a base station. WSNs can be battery-powered or wirelessly powered. Since wirelessly powered WSNs harvest energy from the environment, they do not have to encounter issues regarding the replacement or recharging of batteries. Therefore, they provide significant advantages for sensing in regions that are remote or inaccessible. Additionally, WSNs have the advantage of scalability, which enables the convenient addition or removal of nodes to/from the network. Since WSNs are mostly used in applications where powering them is inconvenient, the major constraint affecting the design of these nodes is low power consumption. Localization is the process of accurately determining the position or location of an object. Localization of WSNs is particularly significant in all these applications to effectively monitor the functionality of these sensors. In this chapter, we focus on two important classes of applications for which localization of WSNs is essential: biomedical and fracture mapping.

1.1 Biomedical applications

Among the variety of applications that require localization of WSNs, biomedical applications form an important class. Battery-powered WSNs have limitations such as the limited lifetime, chemical leakage, and failure of batteries, therefore limiting their use in wearable

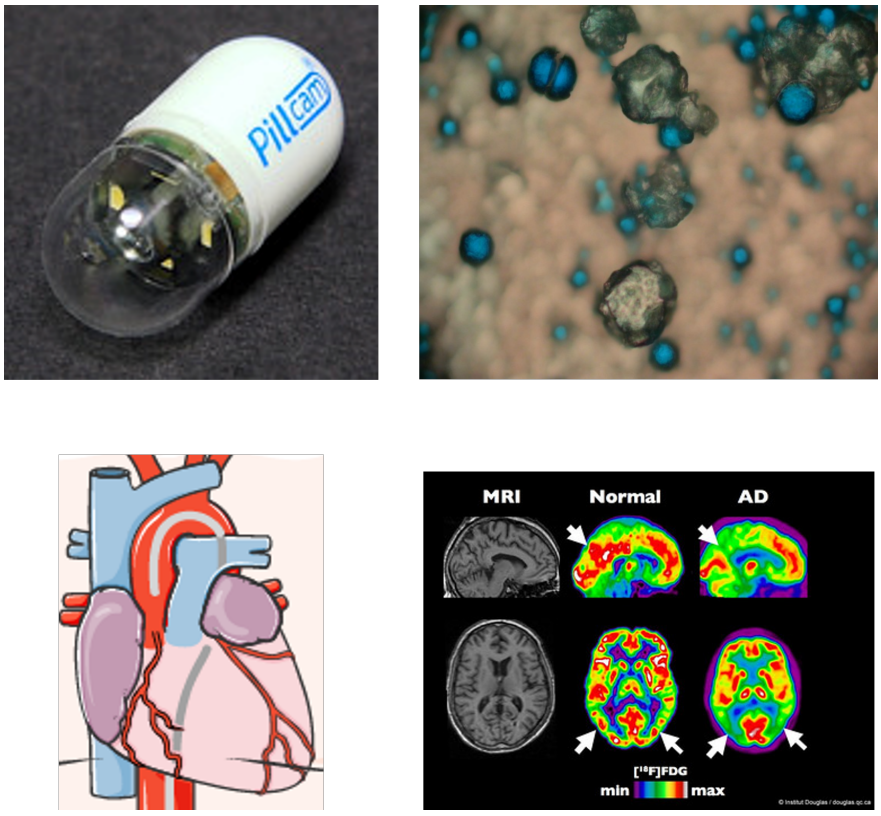

Figure 1.1: Biomedical applications of WSNs

or implantable biomedical applications, leading to wirelessly powered WSNs becoming increasingly popular for these applications. Localization of WSNs is particularly significant for biomedical applications where accurate and precise data collection is essential for monitoring the vital signs of patients to facilitate timely intervention, disease diagnosis, and treatment [4, 5]. Moreover, the constraints imposed by wireless powering have given rise to research focusing on using cheaper methods and more power-efficient hardware to localize these WSNs.

One such application is wireless capsule endoscopy (WCE) for treating gastrointestinal (GI) tract diseases. Conventionally, treatment of GI tract diseases has involved surgical endoscopy, which is performed by inserting probes into the GI tract, causing great pain and inconvenience to the patient. WCE, on the other hand, requires the patient to swallow

capsules, which have the capability to receive and transmit data. These capsules, therefore, provide an alternative painless procedure for monitoring the GI tract. The localization of such capsules, which form the nodes of a WSN, is therefore of paramount importance to provide information about the location of tumors and other abnormalities in the GI tract. Other biomedical applications of localization include automated drug delivery and robotic surgeries [6] in which prior knowledge of the location is crucial. Localization can also become an important feature in implantable biomedical sensors for detecting the location of epileptic electrical activity in the brain [7]. Cardiac ablation procedures [8], which involve inserting catheters into veins or arteries, could also be greatly simplified using the localization of WSNs. Fig. 1.1 depicts the different biomedical applications of WSNs. Therefore, localization has a broad range of biomedical applications that are extremely essential for the advancement of humanity.

Prior work on the localization of WSNs for biomedical applications has broadly focused on two significant approaches: (1) Magnetic localization and (2) Electromagnetic (EM) wave-based localization. Magnetic localization has two major advantages. Due to similar values of permeability in air and animal tissue, there is lesser signal attenuation inside the animal body for low-frequency magnetic fields. Moreover, it does not require the node to be in the line of sight with the transmitter (TX) and the receiver (RX). Therefore, magnetic localization has a higher accuracy as compared to other methods [9,10]. However, the absence of ferromagnetic materials must be ascertained to ensure high accuracy since they interfere with the magnetic field used for localization. Among the EM waves, radio frequency (RF) has most commonly been used. RF-based localization provides savings in hardware compared to magnetic localization using permanent magnets. Using coils to generate magnetic field gradients overcomes this limitation at the cost of a large form factor and generating a large amount of heat for a large field of view (FOV). Therefore, RF-based localization can be implemented with a smaller form factor, and lower cost [9, 10]. However, RF signals are attenuated by different amounts at different locations inside the animal body. Therefore,

proper characterization of the medium is required before localization. The choice of frequency is also important for such methods. Higher frequency signals do not pass through the animal tissue. Lower frequency improves penetrability through animal tissues but reduces accuracy.

Over the years, the rapid scaling of CMOS has enabled a reduction in the IC size and, therefore, that of the nodes used. Today, the size of these nodes is almost entirely dominated by the size of passives. In RF-based localization, the requirements for penetration of RF signals through animal tissue, skin, and bones limit their frequencies to less than a few hundred megahertz (MHz). Reducing the form factor of the localization system requires the design of millimeter-scale coils or antennas. At such frequencies, the constraints on antenna size reduce the efficiency of the wireless link [11, 12]. This entails the usage of either higher TX power or the design of an IC having lower power consumption. The localization accuracy also directly depends on the Signal-to-Noise Ratio (SNR) at the receiver. A larger received signal power is therefore required to obtain an improved SNR. At MHz-range frequencies, the TX and RX antennas are almost always in the near field. Attempts to increase the operating range of the link lead to increased path loss ($\propto 1/r^6$) and, therefore, lesser received power. Therefore, multiple transmitting nodes with the same frequency and phase can be used to increase the received signal power. A conventional technique to do this is using oscillators in phase-locked loops (PLLs) [13] or injection-locked power oscillators [14–16]. PLLs require a crystal oscillator, while injection-locking suffers from limited locking range. Since both these techniques are extremely power-hungry, it is a challenge to synchronize these nodes for low-power applications efficiently.

1.2 Fracture mapping applications

Among the many applications where wireless sensor networks can be used, hydraulic fracturing is essential for its widespread use in the energy industry, especially the oil and gas industry. Hydraulic fracturing has been used to increase the flow rate of oil and natural

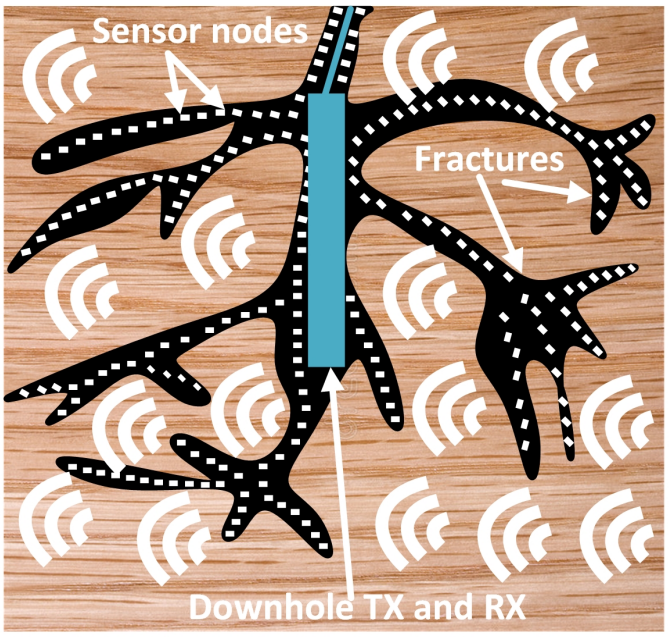

Figure 1.2: Conceptual representation of fracture mapping using WSNs

gas in oilfields [17]. Extensive knowledge about the location and orientation of the fractures is required to increase production efficiency inside these oilfields [18]. Traditionally, fractures have been mapped using techniques such as radionuclide monitoring, where radioactive tracers are injected into the fractures along with the propellant fluid [19]. However, these techniques are prone to high contamination risks if parameters such as the amount, toxicity, and half-life of the tracers are not strictly controlled. More advanced applications use microseismic mapping, which includes monitoring the seismic activities along the fractures and is similar to seismology [20–22]. However, there is not enough understanding of the seismological processes inside the fractures. Moreover, they suffer from coherent noise within the band of seismic recordings. These shortcomings prompt us to look into wirelessly powered WSNs having a small form factor and low power consumption as a cleaner, newer, and more power-efficient technique for fracture mapping. Fig. 1.2 shows a conceptual representation of fracture mapping using WSNs.

Previous systems for fracture mapping have primarily focused on using nanoparticles and

their responses to electromagnetic or acoustic waves inside fractures. [23,24] use paramagnetic nanoparticles for the detection of fractures using susceptibility measurements at different locations. [25] uses a nanofluid and the convection and diffusion processes that affect it, while [26] measures the magnetic anomaly responses due to the injection of magnetic proppant. However, for small fractures, the changes in magnetic susceptibility and fields are weak in the presence and absence of fractures, reducing the accuracy of fracture mapping. To the best of our knowledge, [27] is the only work in literature to date that use WSNs for fracture mapping through a technology called FracBots (Fracture Robots). These FracBots use off-the-shelf components and near-field communication and are placed inside fractures to receive and transmit signals. However, these nodes have a large size, large coils for the RX and TX, and use milliwatt (mW)-level power.

In recent years, hydraulic fracturing has been undertaken in high-temperature rock formations for applications such as obtaining natural gas from unconventional reservoirs [28]. These reservoirs are often located at large depths inside the surface at temperatures close to 250 °C and pressures close to 7 MPa. Ensuring the functionality of the system at high temperatures and pressures is, therefore, an essential part of using WSNs for fracture mapping. Mobility variation, threshold voltage reduction, and junction leakage currents are the major factors affecting the use of standard silicon complementary metal-oxide-semiconductor (CMOS) processes at high temperatures. Therefore, silicon carbide (SiC), silicon-on-insulator (SOI), and other III-V semiconductors were conventionally considered the materials of choice for designing microchips at such temperatures [29–31]. Scaling of CMOS process nodes has resulted in an increase in doping concentration, resulting in lower junction leakage current at high temperatures. However, scaling also results in a lower value of threshold voltage, leading to more channel leakage. Since the junction leakage dominates at high temperatures, standard silicon CMOS processes have been recently used for high-temperature applications in fields such as aerospace, automobile, and deep-well drilling [32–34].

1.3 Organization

The contents of this thesis have already been published in [35–37]. The rest of this thesis is organized as follows. Chapter 2 discusses the design of the wireless power transfer link used in the localization systems. Chapter 3 discusses the design and verification of the wirelessly powered localization and motion detection system for point-of-care biomedical applications. Chapter 4 discusses the wirelessly powered system of coherent sensing nodes for fracture mapping applications at high temperatures and pressures. Chapter 5 summarises the thesis and discusses potential future directions for research.

CHAPTER 2

Wireless Power Transfer Link Design

This chapter describes a detailed qualitative and quantitative analysis of the design of the wireless power transfer link that has been used for the localization systems illustrated in the upcoming chapters.

2.1 Link modeling and coil design

Fig. 2.1 illustrates the circuit model for the wireless power transfer (WPT) link between (a) the TX coil and localizer coil 1 and (b) localizer coil 2 and the RX coil. Since the two links have similar characteristics, only the link shown in Fig. 2.1(a) is analyzed, and the insights obtained have been applied to the design of the other link. The link efficiency (η_{link}) is given by the product of the efficiency of the localizer coil (η_{loc}) and that of the TX coil (η_{TX}) [38]. The maximum η_{TX} is obtained when the operating frequency is equal to the resonant frequency (ω_{res}) of the localizer coil. Since the input resistance of the rectifier (R_{in}) is much larger than the resistance of the localizer coil (R_{loc}), a parallel capacitance C_{par2} is used to resonate the localizer coil at its operating frequency of 40.68 MHz [38]. In such a topology, ω_{res} is given by

$$\omega_{res}^2 = \frac{1}{L_{loc}(C_{par2} + C_{in})}. \tag{2.1}$$

where L_{loc} is the inductance of the localizer coil and C_{in} is the input capacitance of the rectifier as shown in Fig. 2.1(a). Similarly, C_{par3} is used to resonate localizer coil 2 at its

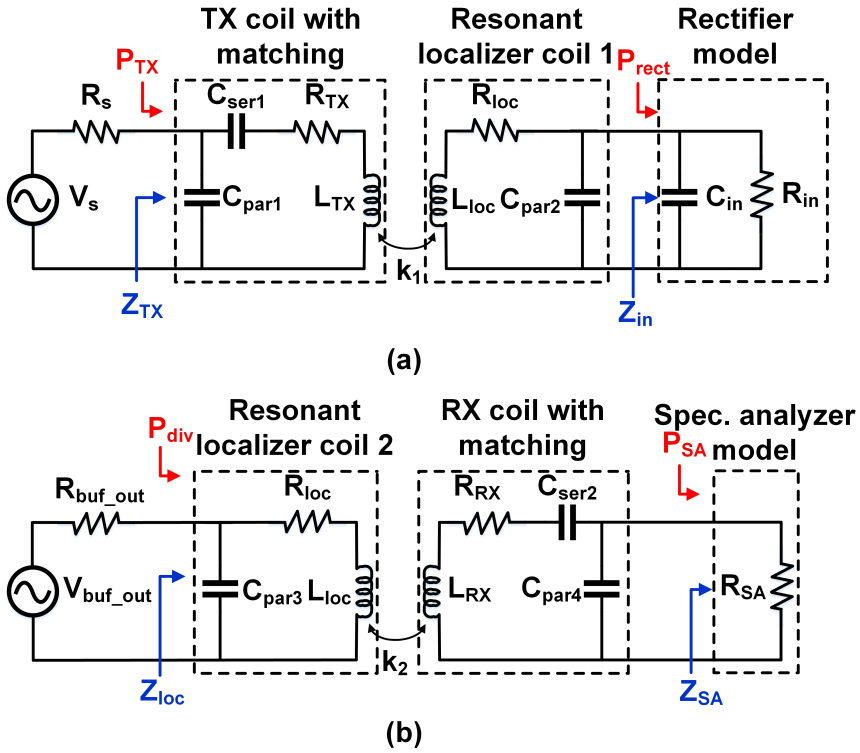

Figure 2.1: Circuit model of the wireless power transfer (WPT) link between (a) TX coil and localizer coil 1 and (b) localizer coil 2 and RX coil

operating frequency of 13.56 MHz. Off-chip ceramic capacitances C_{par2} and C_{par3} of values 16.8 pF and 150 pF respectively were therefore connected in parallel to the localizer coils, improving the power received and transmitted by the localizer at these desired frequencies. η_{loc}, η_{TX}, and η_{link} of the link are then given by [38]

$$\eta_{loc} = \frac{Q_{loc_L}}{Q_{rect}} \tag{2.2}$$

$$\eta_{TX} = \frac{k^2 Q_{TX} Q_{loc_L}}{k^2 Q_{TX} Q_{loc_L} + 1}. \tag{2.3}$$

$$\eta_{link} = \eta_{loc} \eta_{TX}. \tag{2.4}$$

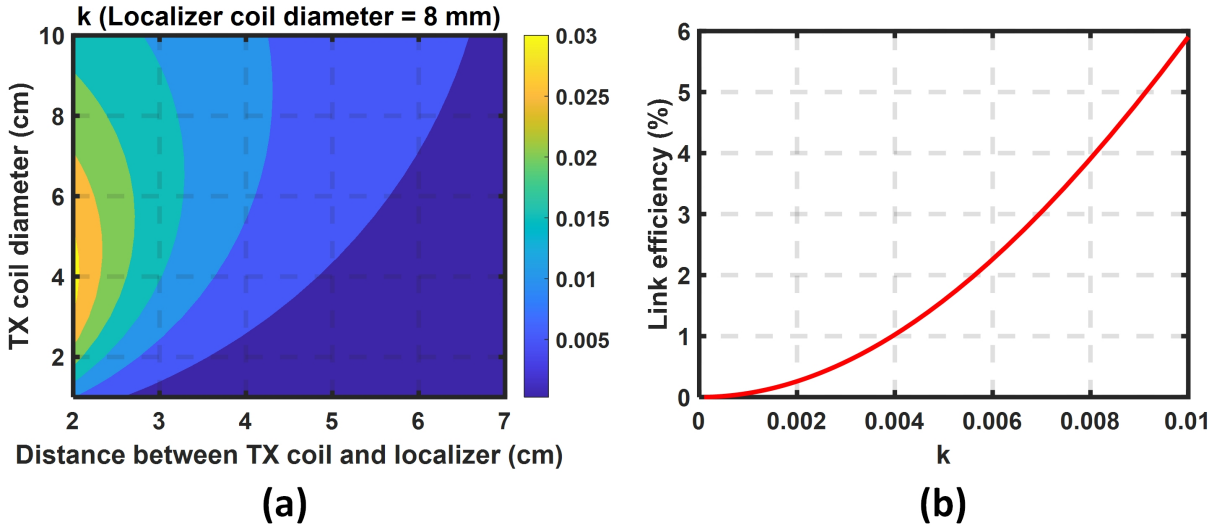

Figure 2.2: (a) Coupling coefficient k between TX coil and localizer coil 1 with respect to the distance between TX coil and localizer for a localizer coil diameter of 8 mm and (b) Calculated link efficiency versus coupling coefficient

where Q_{rect} is the quality factor of the load given by $Q_{rect} = R_{in}/\omega L_{loc}$, Q_{loc_L} is the loaded quality factor of the localizer coil given by $Q_{loc_L} = Q_{loc}Q_{rect}/(Q_{loc}+Q_{rect})$ ($Q_{loc} = \omega L_{loc}/R_{loc}$), Q_{TX} is the quality factor of the TX coil given by $Q_{TX} = \omega L_{TX}/R_{TX}$, and k is the distance-dependent coupling factor between the TX coil and the localizer coil. The coupling factor can be determined from the self and mutual inductances of the coils or can also be empirically given by [38]

$$k = \frac{d_{TX}^2 d_{loc}^2}{8\sqrt{d_{TX}d_{loc}}(D^2 + \frac{d_{TX}^2}{4})^{\frac{3}{2}}}. \tag{2.5}$$

where d_{TX} and d_{loc} are the diameters of the TX coil and localizer coil, respectively, while D is the distance between these coils. The diameter of the localizer coils is constrained to 8 mm to minimize the form factor of the entire system, thereby enabling the use of these localizers in capsules for endoscopy. Fig. 2.2(a) shows the coupling factors obtained using (2.5) for a localizer coil diameter of 8 mm as the diameter of the TX coil and distance between

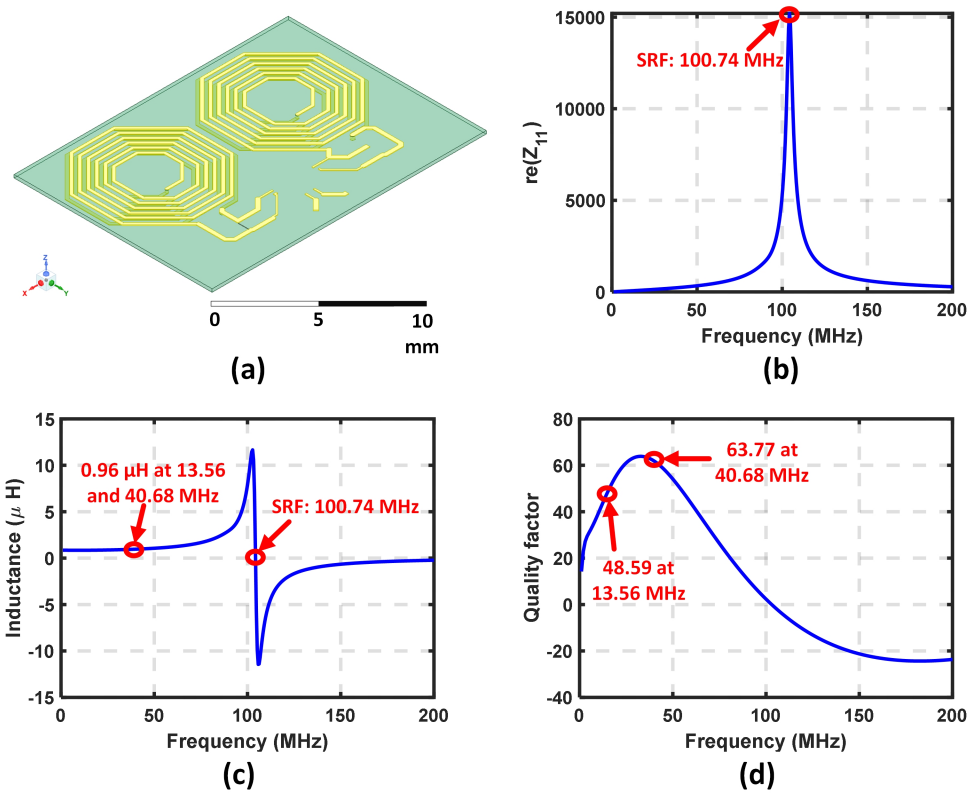

Figure 2.3: (a) HFSS schematic with two localizer coils and the simulated (b) $re(Z_{11})$, (c) inductance, and (d) quality factor of each localizer coil in the absence of a resonating capacitor

the TX coil and localizer are varied. At a distance of 4 cm, a maximum coupling factor of 0.01 can be obtained for a TX coil diameter of 10 cm. The coupling factor also does not change much at larger distances when the diameter of the TX coil is increased. Therefore, a diameter of 3.5 cm is chosen for the TX coil. Fig. 2.2(b) plots the link efficiency calculated using (2.2), (2.3) and (2.4) as a function of the coupling factor at a distance of 4 cm between the TX coil and localizer. The parameters of the designed TX coil and localizer coil given in Table 2.1 have been chosen for this plot. A maximum of 6% link efficiency is obtained for a coupling factor of 0.01.

From (2.4), it can be deduced that the link efficiency increases with an increase in the

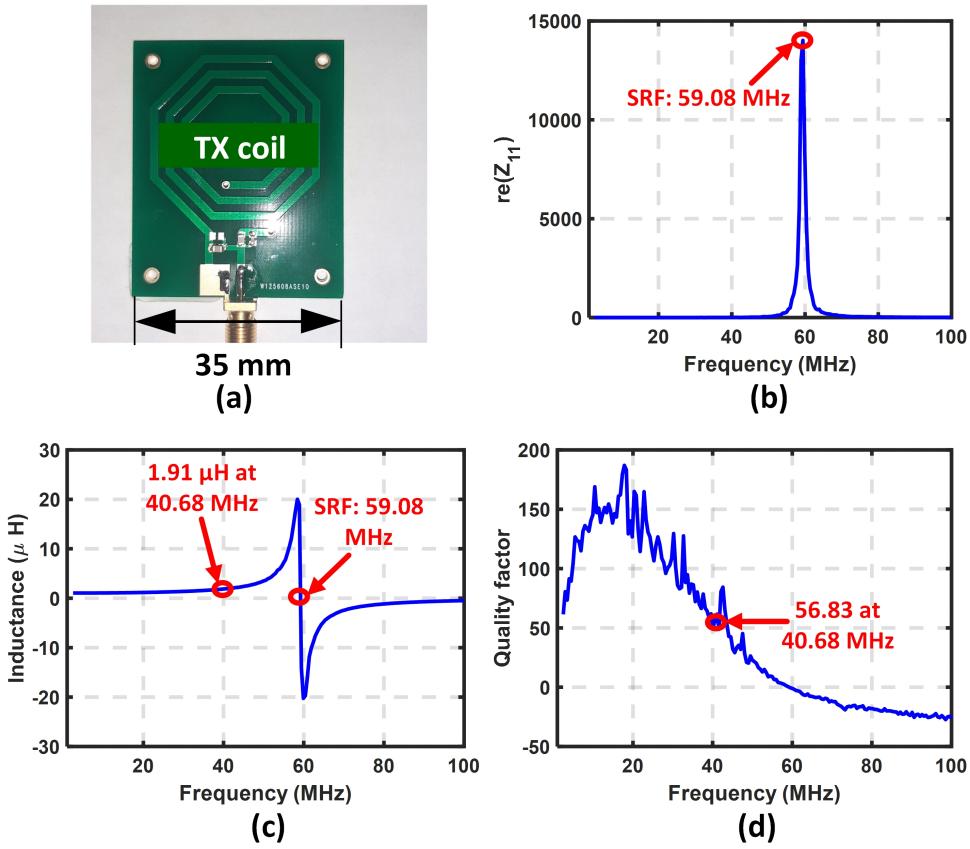

Figure 2.4: (a) TX coil and its measured (b) $re(Z_{11})$, (c) inductance, and (d) quality factor when it is not matched

values of k, Q_{TX} and Q_{loc}. The larger self-inductance of the TX coil and localizer coil improves the link efficiency for wireless power transfer (WPT) by increasing the quality factor of each of these coils. Since the localizer coils have extremely small inductance due to their small diameter, (1) the trace widths of these coils are minimized, (2) the number of turns is maximized, and (3) the thickness of the substrate is reduced to obtain the maximum possible value of inductance. Therefore, these coils are fabricated on a 0.2 mm thick two-layer FR4 substrate with 6 turns on each layer. Since these coils are small, the parasitic inductance of connectors is comparable to the coil inductance, making it unfeasible to measure their s-parameters or inductance using commercially available equipment such as a vector network

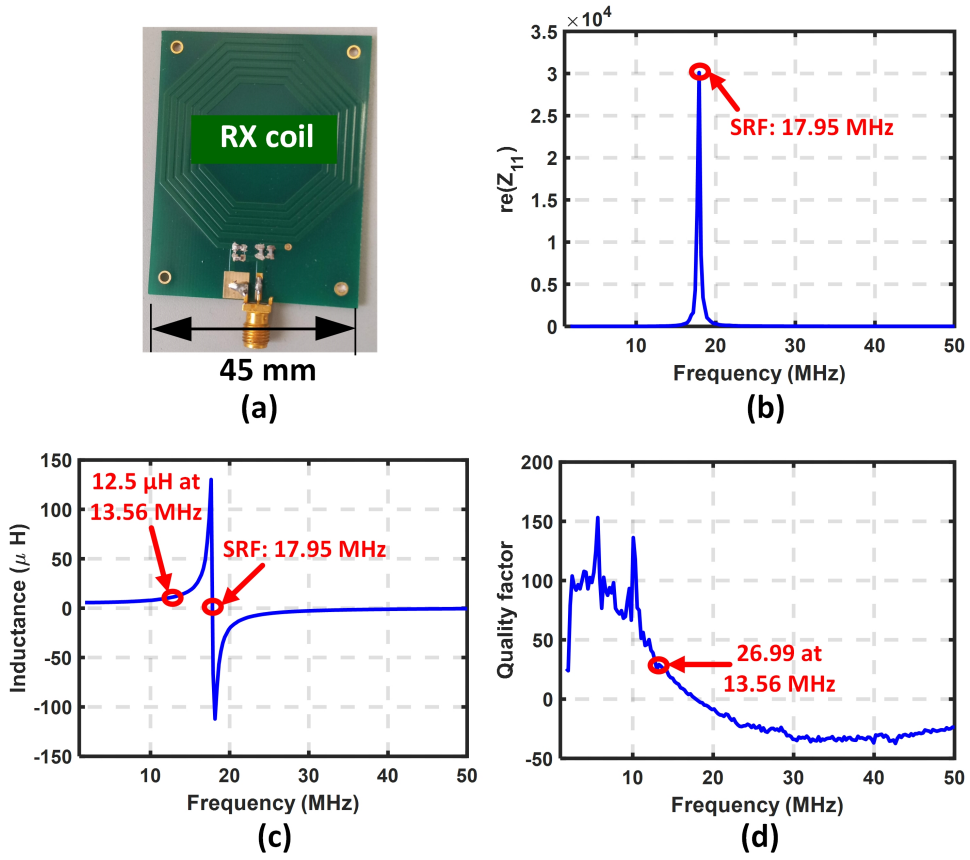

Figure 2.5: (a) RX coil and its measured (b) $re(Z_{11})$, (c) inductance, and (d) quality factor when it is not matched

analyzer (VNA). Fig. 2.3 shows (a) the Ansys HFSS schematic of the localizer and the simulated (b) real part of Z_{11}, (c) inductance, and (d) quality factor of each localizer coil when it is not connected to the resonating capacitance.

The TX and RX coils are designed to have a large quality factor and a self-resonant frequency (SRF) close to the operating frequency to improve the link efficiency. The performance of these coils is measured using a Keysight N5230C PNA-L Network Analyzer. Fig. 2.4 shows the (a) TX coil and its measured (b) real part of Z_{11}, (c) inductance, and (d) quality factor while Fig. 2.5 shows the same parameters for the RX coil. The TX and RX coils are matched to 50 Ω for maximum power transfer. The path loss of the TX and RX

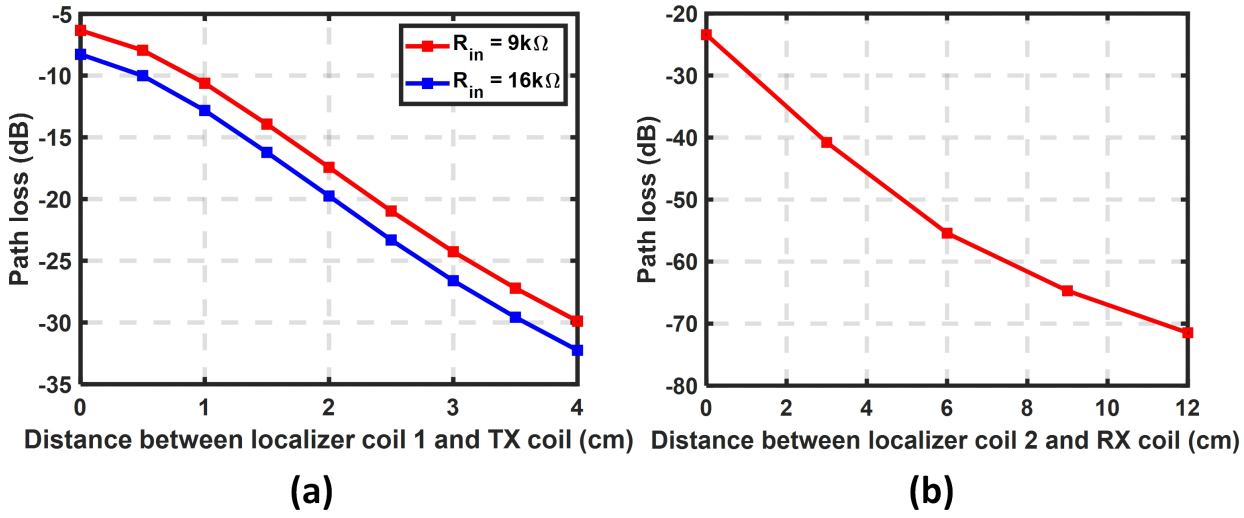

Figure 2.6: Simulated path loss between (a) TX coil and localizer coil 1 at 40.68 MHz for R_{in} = 9 $k\Omega$ and R_{in} = 16 $k\Omega$ and (b) RX coil and localizer coil 2 at 13.56 MHz for R_{buf_out} = 5 $k\Omega$

links is simulated using Ansys HFSS. Fig.2.6(a) shows the simulated path loss between the TX coil and the localizer coil 1 at 40.68 MHz, while Fig. 2.6 (b) shows the simulated path loss between the localizer coil 2 and the RX coil at 13.56 MHz. Since R_{in} varies from 9 $k\Omega$ to 16 $k\Omega$ (as shown in Fig. 3.4(d)) over the range of input powers, the path loss between the TX coil and the localizer coil 1 at 40.68 MHz is simulated for these two values of R_{in} to obtain the possible range of path loss. Moreover, the path loss between the localizer coil 2 and the RX coil is simulated for an R_{buf_out} of 5 $k\Omega$ since it is equal to the simulated output resistance of the buffer (as shown in Fig. 3.8(c)). The distance between the TX coil and the localizer coil 1 is varied from 0 to 4 cm, while that between the RX coil and the localizer coil 2 is varied from 0 to 12 cm. Table 2.1 describes the details of the coil design parameters.

Table 2.1: Design Parameters of Coils Used

	Localizer coil	TX coil	RX coil
Trace width (mm)	0.18	1.1	1.1
Trace separation (mm)	0.26	1.1	1.1
Diameter (mm)	8	35	45
Substrate	FR4	FR4	FR4
No. of layers	2	2	2
Substrate thickness (mm)	0.2	1.6	1.6
Turns per layer	6	3	6
Self-resonant frequency (SRF) (MHz)	100.74	59.08	17.95
Quality factor (Q)	63.77 at 40.68 MHz (simulated) 48.59 at 13.56 MHz (simulated)	44.03 at 40.68 MHz (measured)	26.99 at 13.56 MHz (measured)
Inductance (μH)	0.96 (simulated)	1.91 (measured)	12.5 (measured)
$\|S_{11}\|$ (dB)	NA	-22.73	-15.42

CHAPTER 3

A Fully Wireless and Batteryless Localization System With 50 μm Motion Detection Capability and Adaptive Transmitter Power Control

This chapter describes a detailed qualitative and quantitative analysis of the design and ex vivo verification of a fully wireless and battery-less localization system for different biomedical applications including capsule endoscopy. Fig. 3.1 shows the conceptual representation of the proposed localization system. Moreover, this chapter also presents experimental results based on a technique for sensing and detecting motion as small as 50 μm using the power of the 13.56 MHz received signal. The system has also been verified in vitro to detect the rate of periodic physiological motion and finds use in biomedical motion-sensing applications such as diaphragm motion for respiration rate sensing or throat motion for speech sensing.

The chapter is organized as follows. Section 3.1 discusses the overview of the system architecture. Section 3.2 discusses the details of circuit implementation and simulation results. Section 3.3 describes the measurement setup and results. Finally, Section 3.4 concludes the chapter.

3.1 System Architecture Overview

Fig. 3.2 shows the architecture of a localizer. The localizer includes an integrated circuit (IC) (enclosed by dashed lines) wire bonded on a PCB and two planar coils fabricated on the same

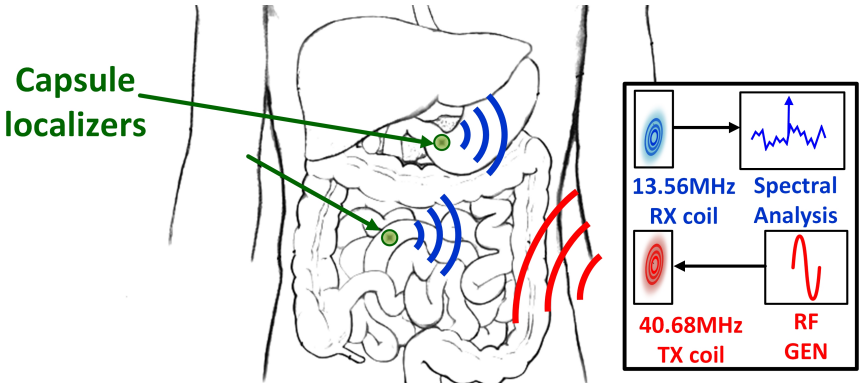

Figure 3.1: Conceptual representation of proposed localization system

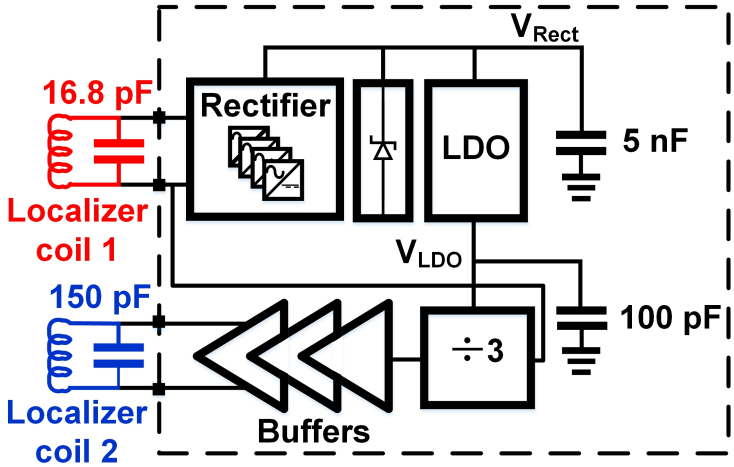

Figure 3.2: Localizer architecture

PCB. Each of these coils has a diameter of 8 mm. The IC comprises a cross-coupled rectifier, an LDO, and a digital divide-by-3 circuit with buffers. The TX coil couples a continuous-wave sinusoidal RF signal at a frequency of 40.68 MHz to localizer coil 1 connected to the input of the rectifier. The RF power is harvested by the rectifier, generating a DC voltage at the input of the LDO. The LDO generates a regulated supply voltage of 1.1 V for the divide-by-3 circuit. The divide-by-3 utilizes the 40.68 MHz TX signal and divides its frequency by 3 to generate a locked sub-harmonic 13.56 MHz signal, therefore eliminating the need for power-hungry oscillators or PLLs. The 13.56 MHz signal at the output of the

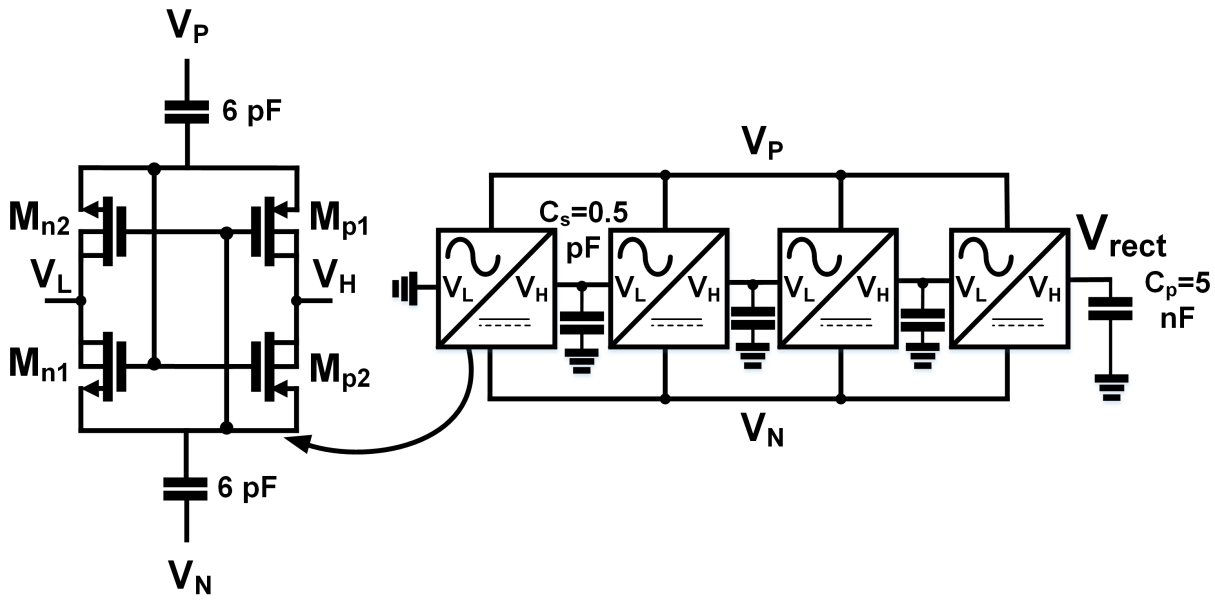

Figure 3.3: Schematic of four-stage passive cross-coupled rectifier

buffers following the divide-by-3 is coupled to the RX coil through localizer coil 2. Using two separate frequencies for transmitting and receiving prevents interference of the received signal with the TX power signal and ensures more localization accuracy. The wireless power transfer (WPT) link is optimized to ensure reliable wireless powering of the system at a maximum distance of 40 mm with 2 W of external power.

3.2 Circuit Implementation

3.2.1 Rectifier

A passive full-wave CMOS rectifier having four stages is used to convert the wirelessly received 40.68 MHz RF signal to a DC voltage. Each stage of the rectifier incorporates a cross-coupled topology, as shown in Fig. 3.3. When V_P is greater than V_N, transistors M_{p1} and M_{n1} are turned on, while transistors M_{p2} and M_{n2} are turned off. The charge on the coupling capacitor connected to V_P is therefore used to charge the output node of the rectifier

stage (V_H). On the other hand, when V_N is greater than V_P, transistors M_{p2} and M_{n2} are turned on, while transistors M_{p1} and M_{n1} are turned off. In this half cycle, the charge on the coupling capacitor connected to V_N is used to charge V_H. The power conversion efficiency (PCE) of a rectifier is the ratio of the power delivered to the load at the output of the rectifier P_{OUT} to the RF power supplied at its input P_{RF}. It is given by

$$PCE = \frac{P_{OUT}}{P_{RF}} = \frac{P_{OUT}}{P_{OUT} + P_{LOSS}}. \tag{3.1}$$

where P_{LOSS} is the effective power loss in the rectifier. An important parameter in the design of the rectifier is its bandwidth given by

$$BW = \frac{f_0}{Q_{rect}} \tag{3.2}$$

where f_0 is the operating frequency and Q_{rect} is the quality factor of the rectifier, as defined earlier. Since C_{in} of the rectifier varies with input power, ω_{res} given by (2.1) also changes. A higher rectifier bandwidth is, therefore, essential for reliable wireless powering of the localizer. The rectifier is simulated for an output voltage of 1.1 V using an input 40.68 MHz RF signal of power ranging from -80 dBm to 0 dBm at a constant load current of 12.75 μA, which is the maximum current that the LDO draws from the rectifier output. Fig. 3.4 illustrates the (a) PCE and (b) bandwidth of the rectifier for different NMOS transistor widths and input powers. Higher PCE is obtained using larger transistors, but the bandwidth drops due to increased input resistance. Therefore, the aspect ratio of NMOS transistors is chosen to be 4 μm / 0.18 μm. The PMOS transistor widths are chosen to be double that of the NMOS transistors. Fig. 3.4 (c) shows the variation in the resonant frequency of the localizer ω_{res} due to the variation in C_{in} of the rectifier with input power, while Fig. 3.4 (d) shows the variation in its input resistance R_{in} for the selected transistor aspect ratio. Since this variation in R_{in} only changes the path loss between the TX coil and the localizer coil 1 by 2 dB (illustrated in Fig. 2.6(a)), it can be concluded that the rectifier has enough

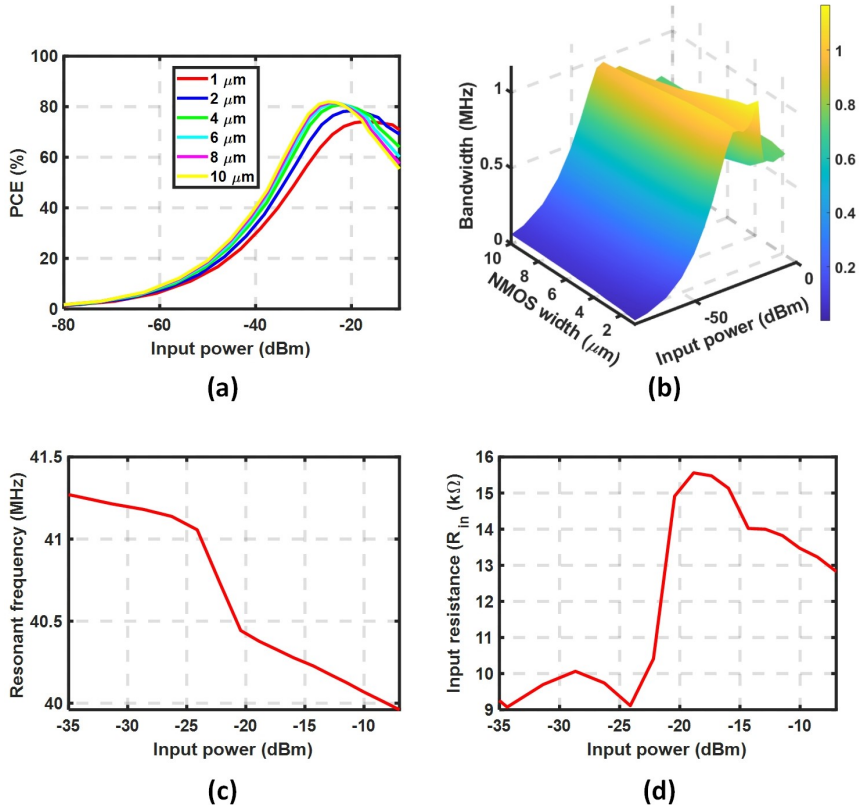

Figure 3.4: Simulated (a) PCE and (b) bandwidth of the rectifier for different transistor widths and input RF powers. (c) and (d) show the variation in localizer resonant frequency (determined by the variation in C_{in}) and variation in R_{in} respectively with different input RF powers for the selected W/L = 4 μm/0.18 μm

bandwidth to withstand the changes in ω_{res}.

Another critical parameter is the sensitivity of the rectifier, which is defined as the minimum RF power required at its input for generating the minimum required voltage at its output for proper operation of the circuit at the desired load. Reducing the rectifier sensitivity is therefore paramount for increasing the link efficiency and, subsequently, the operating range of the wireless power transfer (WPT) system. In this work, the cross-coupled topology is chosen due to its superior sensitivity and PCE among its counterparts [39, 40]. Deep n-well NMOS transistors are used to enable the connection between source and bulk, re-

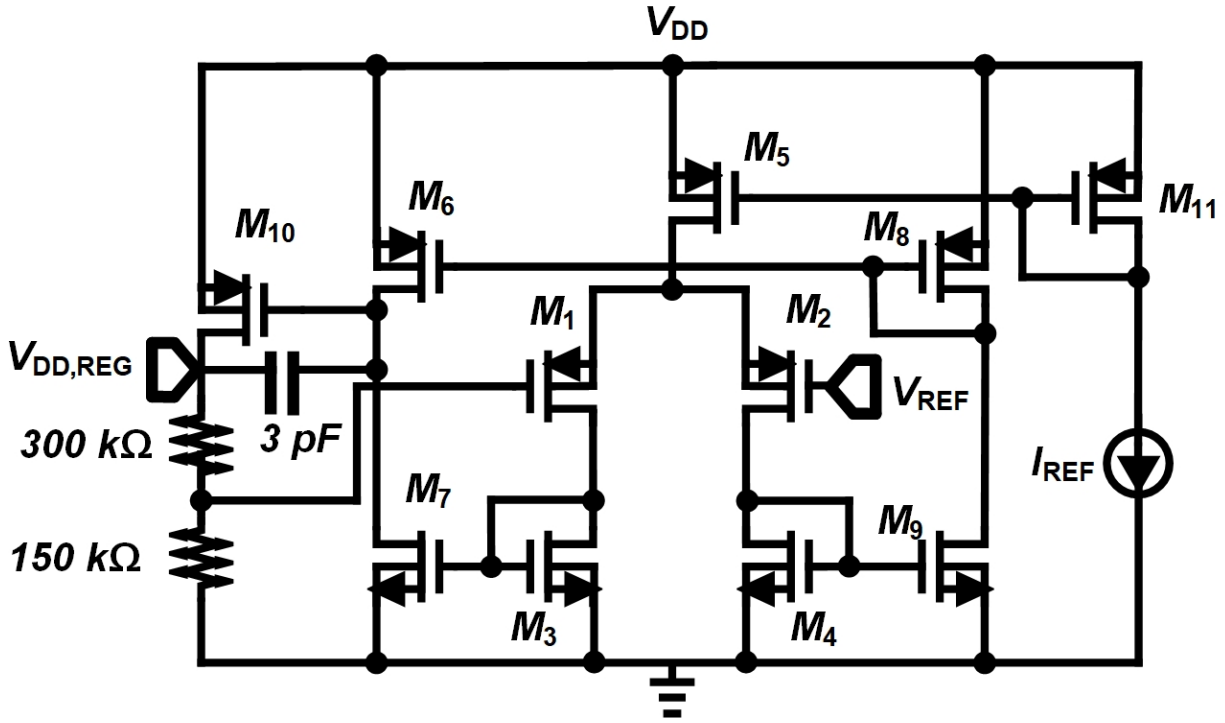

Figure 3.5: Schematic of the LDO

ducing the source-bulk potential for the subsequent rectifier stages and, consequently, the threshold voltage, leading to better sensitivity and PCE. As mentioned in Section 3.2.2, an LDO output voltage of 1.1 V is targeted, while the LDO has a dropout voltage of 47.64 mV. Therefore, the minimum rectifier output voltage for proper operation is approximately equal to 1.16 V. The sensitivity of the rectifier simulated at an output voltage of 1.16 V and a load current of 12.75 μA is obtained to be equal to 32 μW. For each stage, coupling capacitors of 6 pF are chosen to couple the signal to the input of the rectifier with an attenuation of less than 1 %. A 5 nF on-chip storage capacitor C_p is used to reduce the ripple at the output of the rectifier. A diode limiter is used to limit the rectifier output voltage V_{rect} to less than 3.8 V, therefore preventing the breakdown of transistors.

3.2.2 Low-dropout regulator (LDO)

The output of the rectifier acts as the line voltage of the LDO. The LDO is required to generate a regulated DC voltage of 1.1 V at its output, which is used as the supply voltage for the IC. Fig. 3.5 depicts the schematic of the LDO. It includes an error amplifier that compares a reference voltage (V_{REF}) of 336 mV and the voltage generated by the resistive division of the output. The reference voltage is generated using a bandgap reference generator with proportional-to-absolute-temperature (PTAT) architecture. The pass transistor of an LDO can either be a PMOS device acting as a voltage-controlled current source (VCCS) or an NMOS device acting as a source follower. LDOs with current source pass transistors have higher loop gain and lower dropout voltage as compared to those with source followers [41]. Therefore, an LDO with a current source is used in the design. The pass transistor in such a topology is typically a large device to reduce the dropout voltage [41]. The pass transistor is therefore sized appropriately to generate a low dropout voltage at the highest load current, and the feedback resistor values of 300 and 150 $k\Omega$ are chosen to minimize quiescent power consumption. The LDO requires a smoothing capacitor of 100 pF at its output, which can easily be implemented on-chip. For an LDO with an on-chip output capacitor, the worst-case stability condition occurs when the load current is zero. Therefore, based on the value of the smoothing capacitor, a 3 pF Miller compensation capacitor is chosen to ensure LDO stability under the zero-load current condition. Fig. 3.6(a) and (b) show the simulated magnitude and phase of the loop gain of the LDO, respectively, under two conditions: zero and 10 μA load current. It can be observed from Fig. 3.6 that the LDO has a low-frequency loop gain of 31.53 dB and a phase margin of 57.79 degrees at a unity-gain bandwidth of 21.14 kHz when the load current is zero. The loop gain drops to 30.3 dB, and the unity-gain bandwidth increases to 25.22 kHz when the load current is 10 μA.

Specifications of the LDO include the quiescent current consumption, which is the static current consumed by the LDO when the load current is zero. Line and load regulations are other important specifications that quantify the variation in the LDO output voltage with

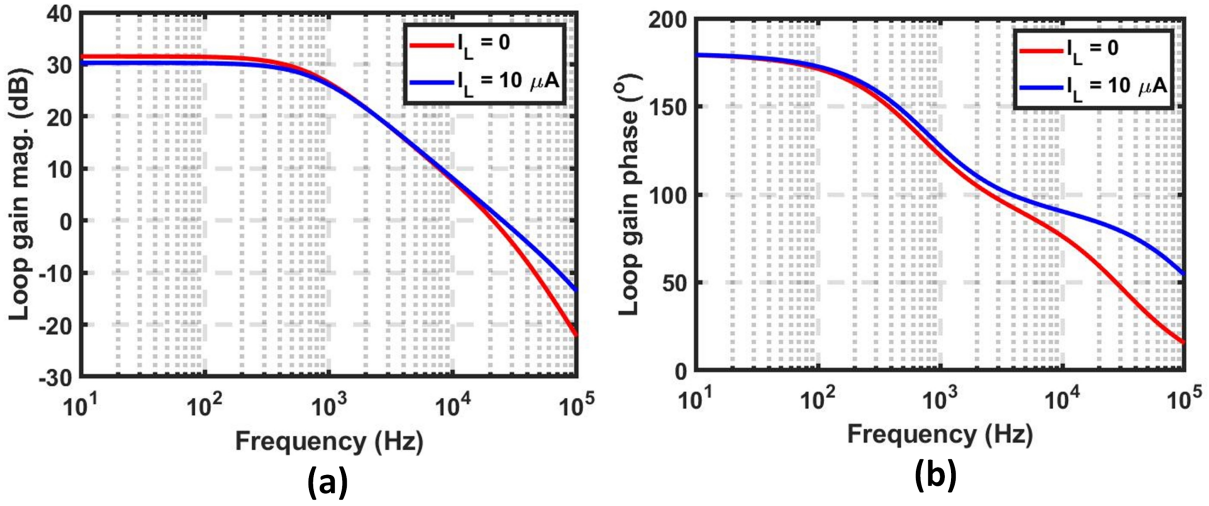

Figure 3.6: Simulated loop gain (a) magnitude and (b) phase of the LDO

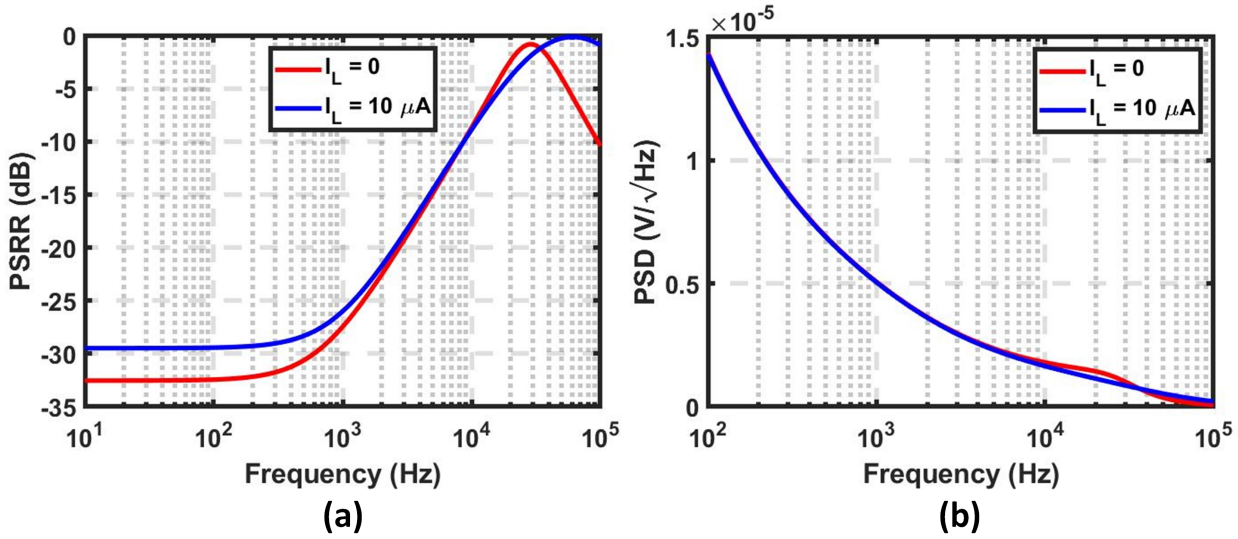

Figure 3.7: Simulated (a) PSRR and (b) power spectral density of output noise for the LDO

changes in line voltage and load current at steady state and are defined as

$$Line\ Regulation = \frac{\Delta V_{LDO}}{\Delta V_{Rect}}\bigg|_{t\to\infty} \times 100\%. \tag{3.3}$$

Table 3.1: Summary of LDO Specifications

Parameter	Value
Preset output voltage (V_{LDO})	1.1 V
Load current (I_L) range	0-10 μA
Dropout voltage	47.64 mV at $I_L = 10\mu A$
Quiescent current (I_Q)	2.75 μA
Line Regulation	<0.2% for both $I_L = 0$ and $10\mu A$
Load Regulation	562Ω
PSRR ($I_L = 10\mu A$)	-29.48 dB at 10 Hz -26 dB at 1 kHz -8.9 dB at 10 kHz
PSRR ($I_L = 0$)	-32.53 dB at 10 Hz -27.46 dB at 1 kHz -8.9 dB at 10 kHz
PSD of output noise	14.31 $\mu V/\sqrt{Hz}$ at 100 Hz 0.22 $\mu V/\sqrt{Hz}$ at 100 kHz

$$Load\ Regulation = \frac{\Delta V_{LDO}}{\Delta I_{LOAD}}\bigg|_{t\to\infty}. \tag{3.4}$$

The load regulation of the LDO is related to its closed-loop DC output resistance. The power supply rejection ratio (PSRR) measures the amount of ripple at the output of the LDO due to a ripple at its input. Therefore, the line regulation of an LDO is equal to its PSRR at DC. Fig. 3.7(a) shows the simulated PSRR of the LDO, while Fig. 3.7(b) shows the power spectral density (PSD) of the noise at the LDO output. Table 3.1 summarizes the specifications of the LDO.

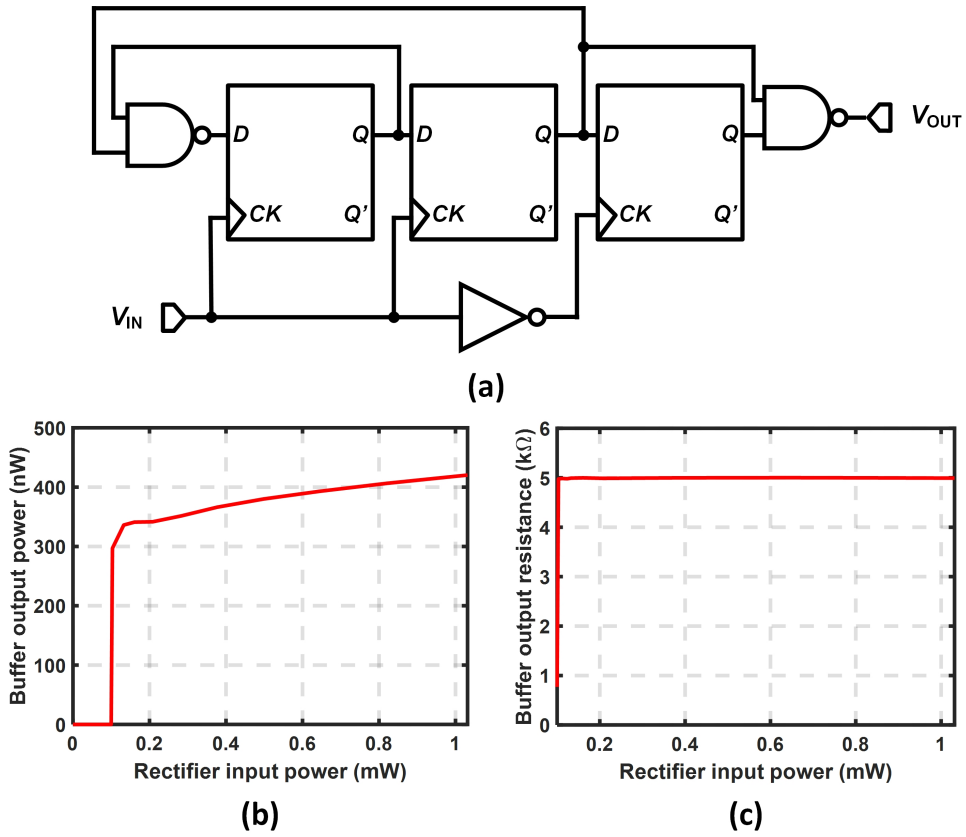

Figure 3.8: (a) Schematic of the divide-by-3 circuit; (b) Output power of the buffer versus rectifier input power, when the buffer is loaded by the circuit parameters of the localizer coil 2 and (c) Output resistance of the buffer versus rectifier input power

3.2.3 Divide-by-3 and buffers

Fig. 3.8(a) shows the schematic of the divide-by-3 circuit. It includes a mod-3 counter and an additional D flip-flop to generate a 50 % duty cycle signal at its output. The designed flip-flops are conventional master-slave flip-flops and have an asynchronous set-reset functionality. The divide-by-3 circuit consumes 1 μW power. Fig. 3.8(b) depicts the power at the output of the buffer following the divide-by-3 circuit with respect to the input power of the rectifier when the buffer is loaded with the circuit parameters of localizer coil 2. The sensitivity of the localization system is determined by that of the rectifier and the divider-buffer combination.

The sensitivity of the rectifier has already been defined earlier. The sensitivity of the divider-buffer combination, on the other hand, is defined as the minimum power at the input of the rectifier for which it generates a detectable 13.56 MHz signal at the output of the buffer. From Fig. 3.8(b), it can be observed that the sensitivity of the divider-buffer combination is 99 μW. The sensitivity of the divider-buffer combination, therefore, dominates over that of the rectifier. Fig. 3.8(c) shows the output resistance of the buffer with respect to the input power of the rectifier. It can be observed that once the divider-buffer combination turns on, the buffer has a constant output resistance of around 5 $k\Omega$.

3.3 Measurement Results

3.3.1 IC functionality verification

Fig. 3.9 shows the die micrograph of the IC in the proposed system. The IC has dimensions of 1.65 mm $\times$ 1.15 mm and is fabricated using TSMC 0.18 μm process. In a separate setup for wired measurements, a 40.68 MHz RF signal was connected to the input of the rectifier using an RF generator (Agilent 33250 A). The voltage at the output of the rectifier and the LDO were then measured using an oscilloscope. Fig. 3.10(a) shows the rectifier and LDO output voltages with respect to input rms voltage. The rectifier output voltage increases with an increase in the input rms voltage, and the rate of increase starts to reduce after a certain input rms voltage. This is due to the reduction in PCE of the rectifier as the input power is increased. The LDO generates a stable DC voltage of 1.05 V for an input rms voltage above 0.8 V. The LDO output voltage is close to the simulated value of 1.1 V. The total simulated power consumption of the IC is equal to 6 μW. Fig. 3.10(b) shows the breakdown of the power consumption of the IC, which is dominated by the LDO.

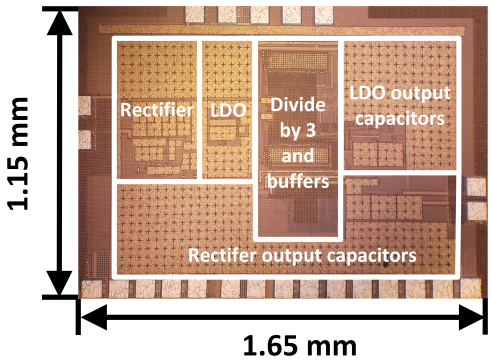

Figure 3.9: Die micrograph of the IC

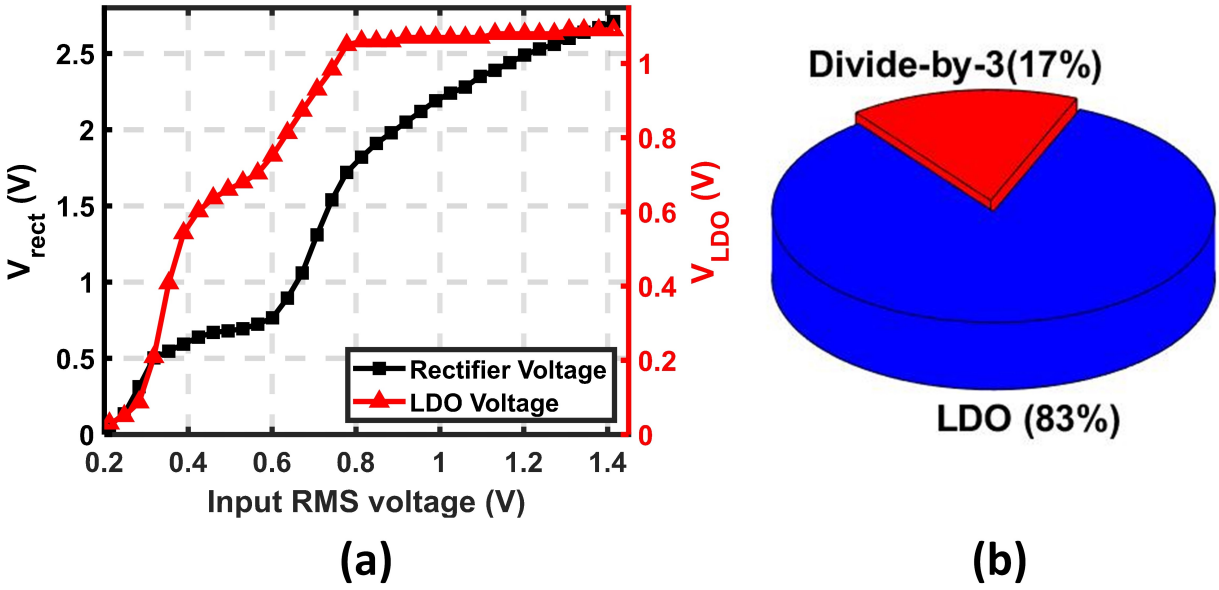

Figure 3.10: (a) Measured rectifier and LDO output voltages versus input rms voltages (b) Breakdown of simulated power consumed by the IC. Total power consumption: 6 μW

3.3.2 Localization system verification

Fig. 3.11(a) illustrates the measurement setup for verifying the proposed localization system. The objective of this measurement was to ascertain the position of two localizers at known locations. Therefore, the localizers are placed on a surface, and one edge of the surface is fixed to be the origin. The centers of the localizers are fixed at known coordinates of (40,

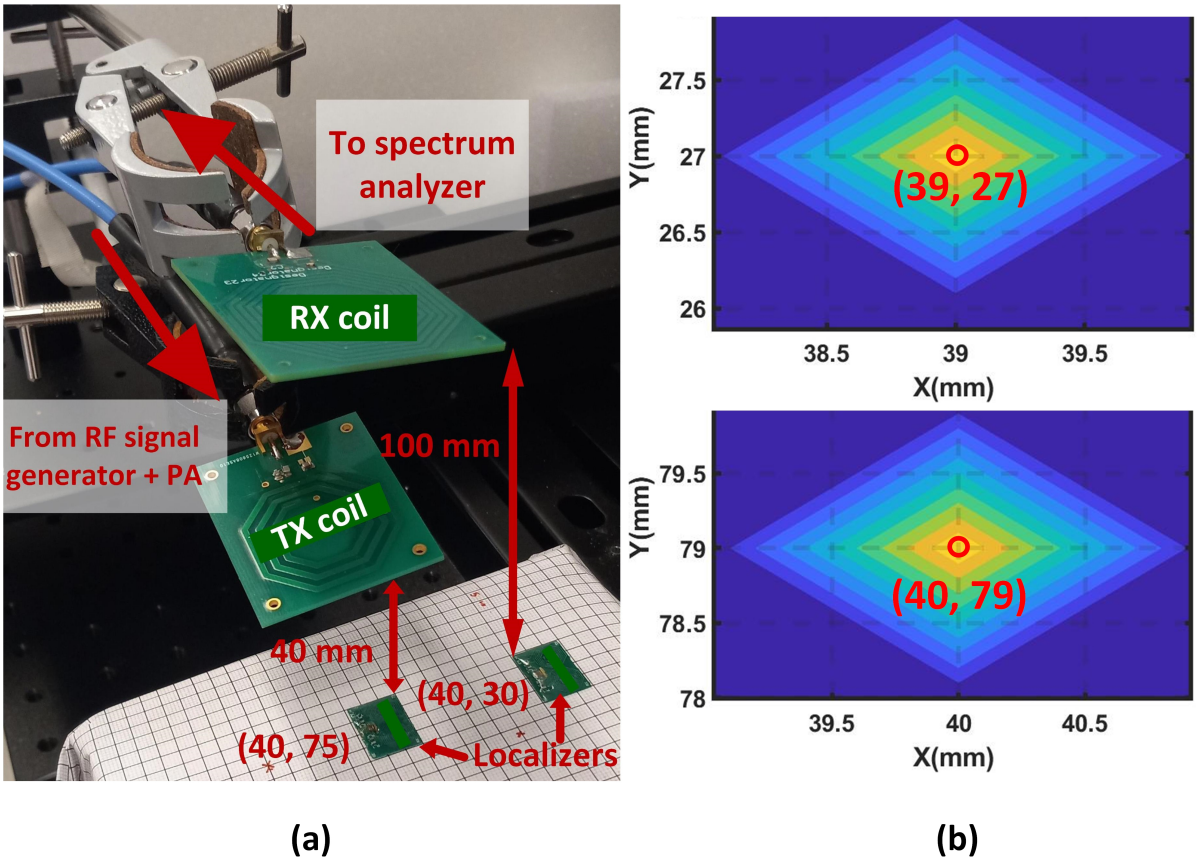

Figure 3.11: (a) Measurement setup for verifying the proposed localization system (b) Coordinates for the center of the localizers at (40, 30) mm (top) and (40, 75) mm (bottom)

30) mm and (40, 75) mm. A 40.68 MHz RF signal having -20 dBm power is generated using the RF signal generator. A power amplifier (PA) (Minicircuits ZHL-20W-13+) was connected in cascade with the RF signal generator to increase the operating range of the wireless link. The PA has a small-signal gain of 50 dB and a saturated output power of 43 dBm. Therefore, the boosted RF signal of 30 dBm power is delivered to the TX coil for wireless powering of the IC. The TX coil is placed at a distance of 4 cm from the localizers. The localizers generate the divide-by-3 signal and transmit back the 13.56 MHz signal to the RX coil, which is placed at a distance of 10 cm from the localizers. Motorized rails

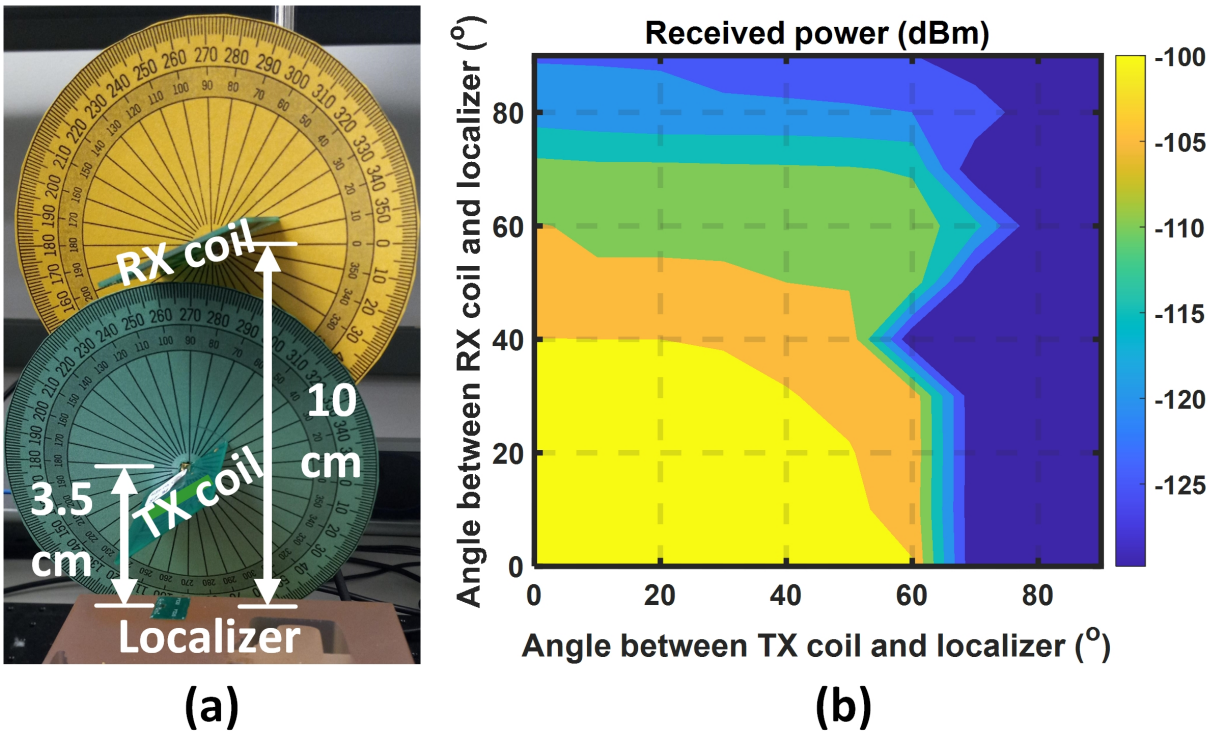

Figure 3.12: (a) Measurement setup used for obtaining received power profile with respect to different angular orientations of the TX and RX coil (b) Received 13.56 MHz signal power in dBm across different angular orientations of the TX and RX coil

(Thorlabs LTS300) are interfaced with MATLAB and used to automate the simultaneous movement of the TX and RX coils to scan the entire area with a 1 mm resolution in the X and Y directions. At each coordinate, the spectrum is recorded using a spectrum analyzer (Keysight PXA Signal Analyzer N9030A) connected to the RX coil. The spectrum analyzer is also interfaced with a laptop for data processing using MATLAB. The coordinate with the maximum received signal power is extracted as the experimentally obtained locations. Fig. 3.11(b) depicts the extracted coordinates obtained for the localizers placed at (40, 30) mm and (40, 75) mm. The obtained coordinates have an error of less than 5 mm.

Using a measurement setup illustrated in Fig. 3.12(a), two paper protractors are added around the TX and RX coils, and the coils are then rotated to measure the received power of

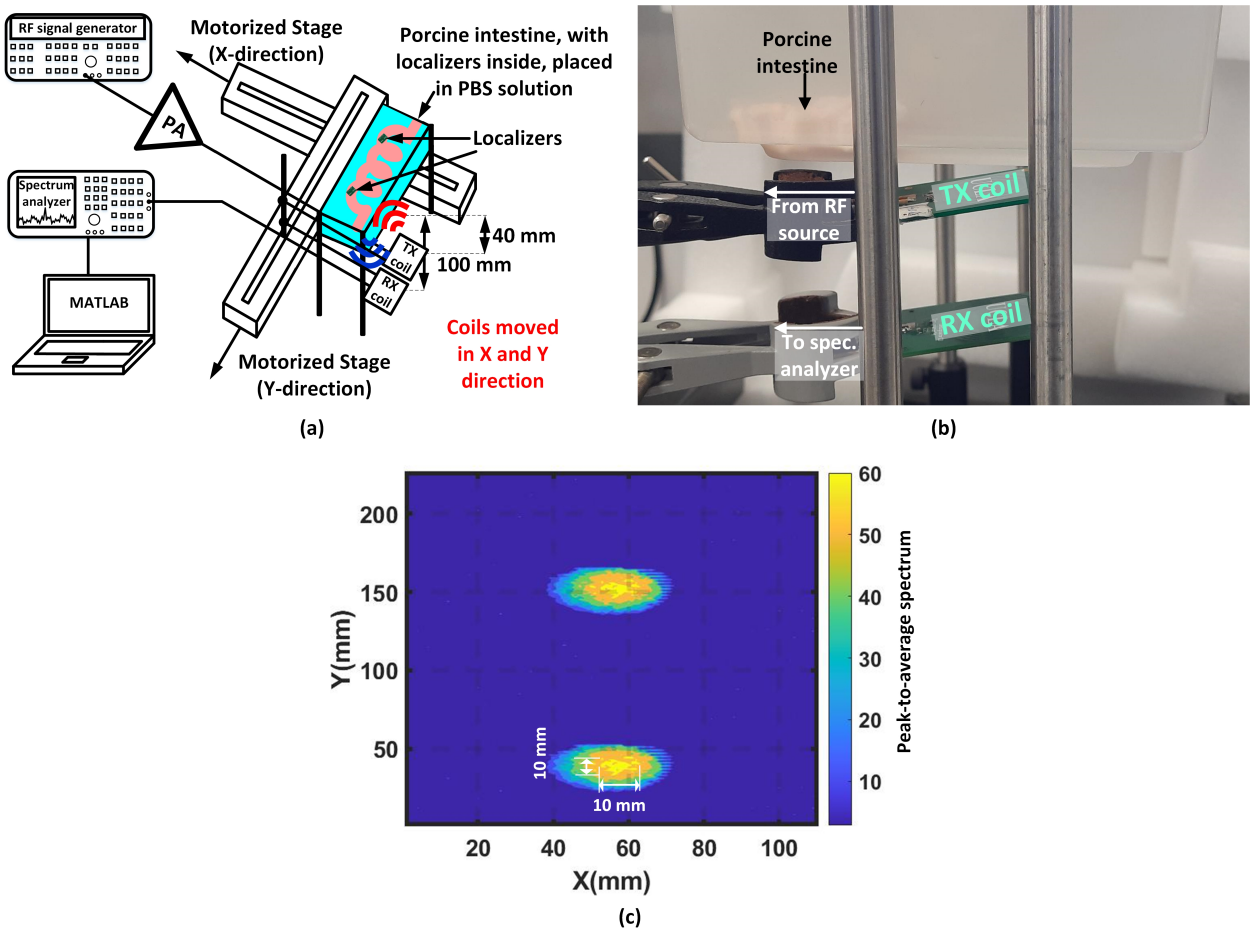

Figure 3.13: (a) Schematic and (b) picture of the setup for ex vivo verification of the proposed localization system inside porcine intestine; (c) Contour plot of the peak-to-average spectrum of the spectrum received at each coordinate. The brighter regions indicate a greater magnitude of the received 13.56 MHz signal

the 13.56 MHz signal at different angular orientations of the TX and RX coils with respect to the localizer. For the purpose of this experiment, a separation of 3.5 cm is used between the TX coil and the localizer, while a separation of 10 cm is used between the RX coil and the localizer. The noise floor for these measurements is observed to be at -128 dBm. Fig. 3.12(b) illustrates the contour plot of the received power across different angular orientations. In case of misalignment between the TX/RX coil and the localizer, it can be observed that

the received power (and consequently SNR) reduces, but this does not affect the spread of the received power, which is determined by the size of the localizer coils. Therefore, the misalignment does not increase localization error. If the minimum SNR required is constrained to 20 dB (chosen only for the purpose of quantifying an acceptable level of misalignment), it can be observed that the system is fairly robust to angular misalignments of up to 60° between the TX coil and localizer and up to 70° between the RX coil and localizer. Increasing (decreasing) the minimum SNR requirement leads to the detection of the 13.56 MHz tone for smaller (larger) angular misalignments between the TX/RX coil and the localizer.

A measurement setup illustrated by Fig. 3.13(a) is used for ex vivo verification of the localization system using porcine intestine. Two localizers are placed in an unknown location inside the porcine intestine, and the intestine is placed inside a container filled with phosphate-buffered saline (PBS) solution. This is done to mimic the characteristics of animal tissue closely. The localizer is encapsulated with a thick layer of ultraviolet (UV) light-cured epoxy resin (BONDIC) before being used for the ex vivo measurement to prevent water and/or PBS solution from leaking into the microchip and causing electrostatic discharge (ESD). A 40.68 MHz RF signal of 36 dBm power is used in this experiment for wireless powering of the IC. A higher power is required due to the extra attenuation of the RF signal as it passes through the bottom of the container, PBS solution, and the intestine. The TX and RX coils were automated to move simultaneously using motorized rails with a resolution of 1 mm in both X and Y directions to scan the bottom surface of the container. Fig. 3.13(b) shows a picture of the measurement setup. At each coordinate, the spectrum is recorded by the spectrum analyzer and sent to MATLAB for processing. The peak-to-average ratio of the spectrum is used to quantify the strength of the received 13.56 MHz tone with respect to the noise floor. Fig. 3.13(c) shows the contour plot of the entire area constructed using peak-to-average values of the received spectrum at each coordinate. Assuming the estimated location of the localizers to be within the region with the brightest contour, the maximum

possible localization error in both dimensions for the raw data is ±5 mm. The error depends on the spatial region where there is sufficient coupling between the TX/RX coil and the localizer coil. Since the localizer coils are much smaller than the TX/RX coils, the detection error is strongly related to the physical size of the localizer coils (which have a radius of 4 mm). It is important to note that the maximum error, in this case, is limited by the diameter of the localizer coil. Therefore, a smaller error could be obtained if a smaller localizer coil is used to transmit back. However, a smaller coil might lead to a reduction in the operating range of the system.

3.3.3 Physiological motion sensing

3.3.3.1 Sensing the rate of motion

The functionality of sensing the rate of physiological motion is verified using the measurement setup as shown in Fig. 3.14 (a). In two different variations of the measurement, the localizer is placed in (i) air and (ii) PBS solution and periodically moved up and down by 4 mm at rates of (a) 10 and (b) 5 beats per minute using a motorized rail (Thorlabs LTS300). Fig. 3.14 (b) shows the picture of the setup when the localizer is placed in air, while (c) shows the picture when the localizer is placed in PBS solution. Similar to the previous experiment, a 40.68 MHz RF signal of 36 dBm power is delivered to the TX coil for wireless powering. The TX and RX coils are kept in a fixed position during this measurement, at average distances of 4 cm and 10 cm, respectively, from the localizer. The spectrum analyzer, connected to the RX coil, records the variation of the received spectrum around 13.56 MHz with time for the entire duration of this measurement. Figs. 3.15(a) and (b) show the received spectrogram for the motion rates of 10 and 5 beats per minute, respectively. For the measurements in both air and PBS, the magnitude and phase information of the spectrogram is then lowpass filtered to remove the 60 Hz supply noise, and the motion rate is extracted using MATLAB.

Fig. 3.16 (a) and (b) depict the signal power magnitude obtained from the magnitude of

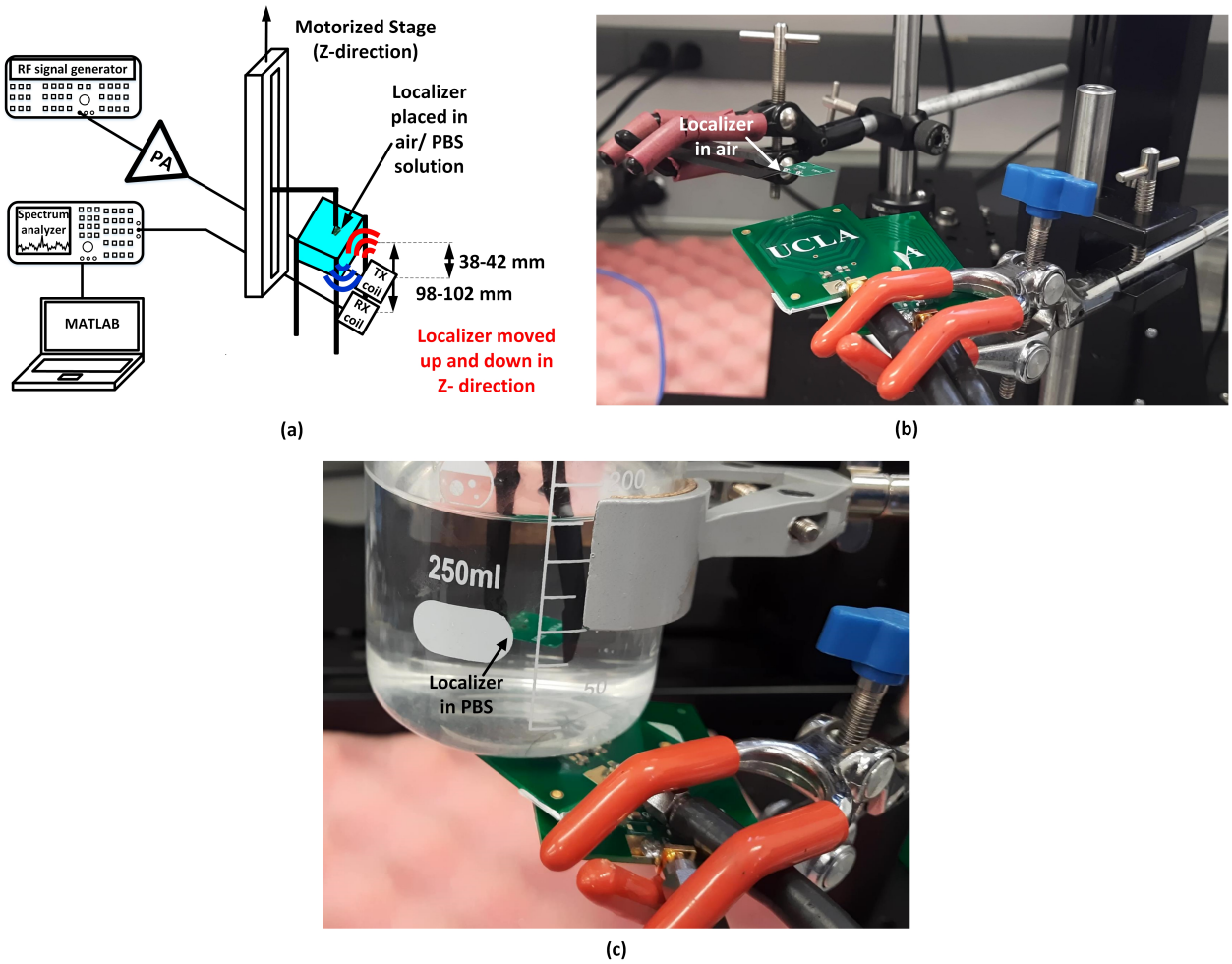

Figure 3.14: (a) Schematic of the measurement setup for sensing the rate of physiological motion; (b) picture of the setup when localizer is in air and (c) when it is in PBS solution

the received spectrogram when the localizer is placed in air and PBS solution, respectively. It can be observed that the received signal power is around 90 pW when the coils are closest to the localizer and drops to almost zero when the coils are farthest. Fig. 3.16 (c) and (d) depict the extracted motion rates from the received signal power when the localizer is placed in air and PBS solution, respectively. Fig. 3.17 (a) and (b) depict the frequency noise obtained from the phase of the received spectrogram when the localizer is placed in air and PBS solution, respectively. The frequency noise is defined as the difference between the

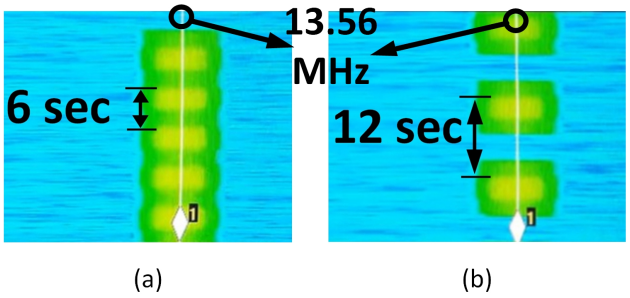

Figure 3.15: Spectrogram for motion rates of (a) 10 and (b) 5 beats per minute. Brighter regions indicate a stronger received 13.56 MHz tone

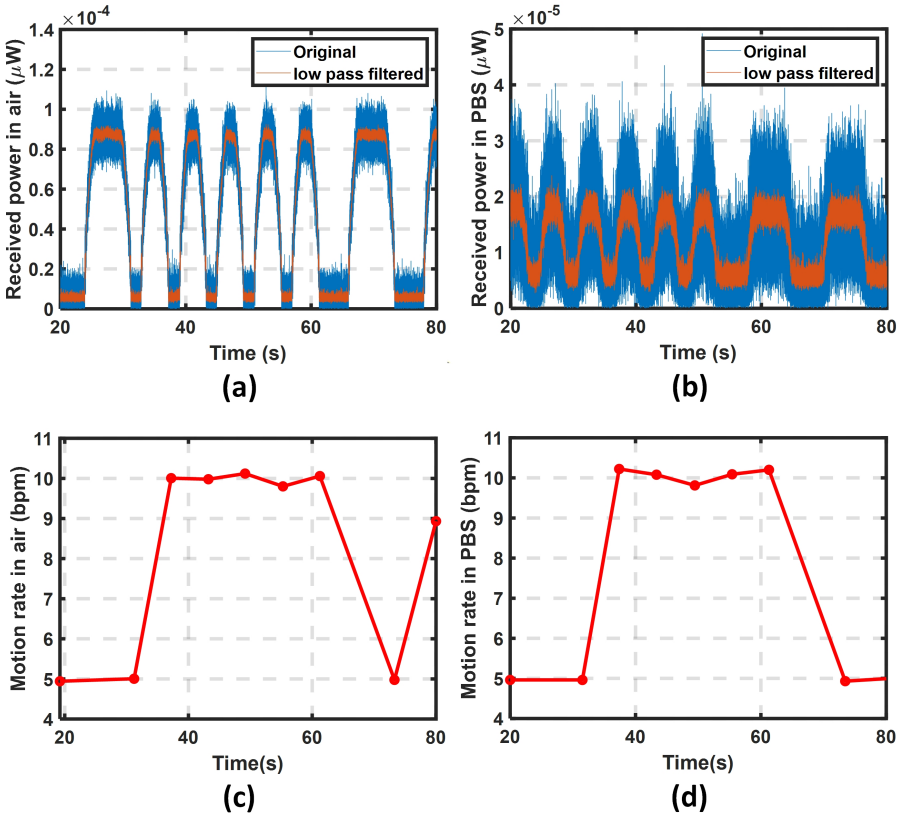

Figure 3.16: Received signal power magnitude from the spectrogram when the localizer is placed in (a) air and (b) PBS solution before and after filtering; Extracted motion rates in (c) air and (d) PBS solution

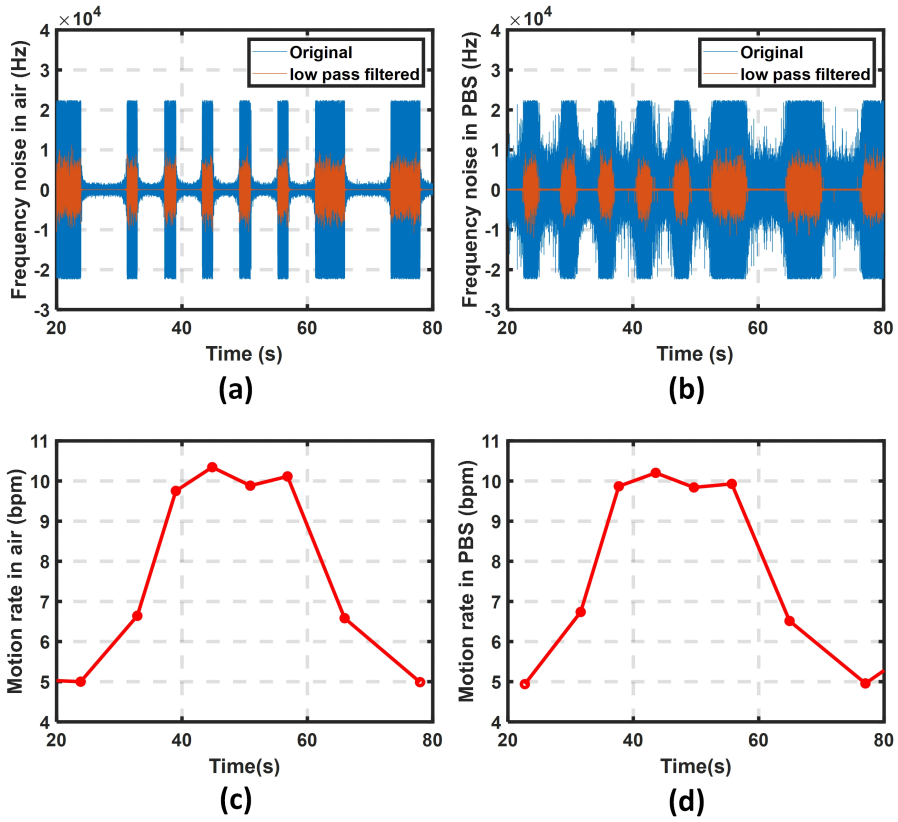

Figure 3.17: Frequency noise in the received spectrogram when the localizer is placed in (a) air and (b) PBS solution before and after filtering. The frequency noise is more when the localizer is not powered; Extracted motion rates when the localizer is placed in (c) air and (d) PBS solution

expected signal frequency (13.56 MHz) and the frequency of the maximum tone received. It can be observed that the frequency noise is much larger when the coils are farthest from the localizer because the localizers are not powered in this position, and the received signal almost entirely consists of noise. The frequency noise is much lesser when the coils are closest to the localizer. Fig. 3.17 (c) and (d) depict the extracted motion rates from the frequency noise of the received signal when the localizer is placed in air and PBS solution, respectively.

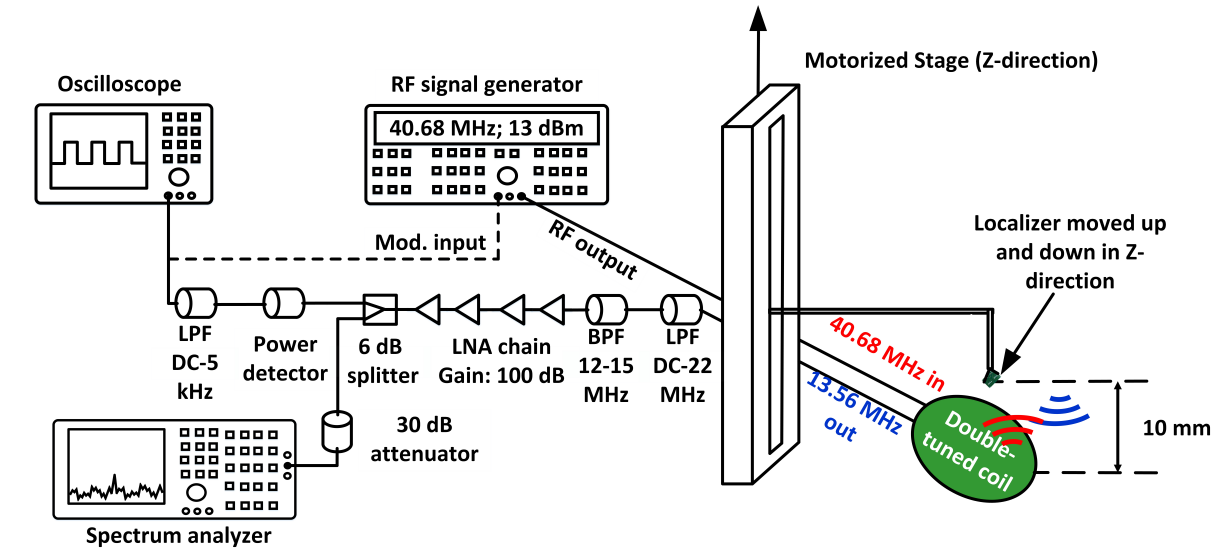

(a)

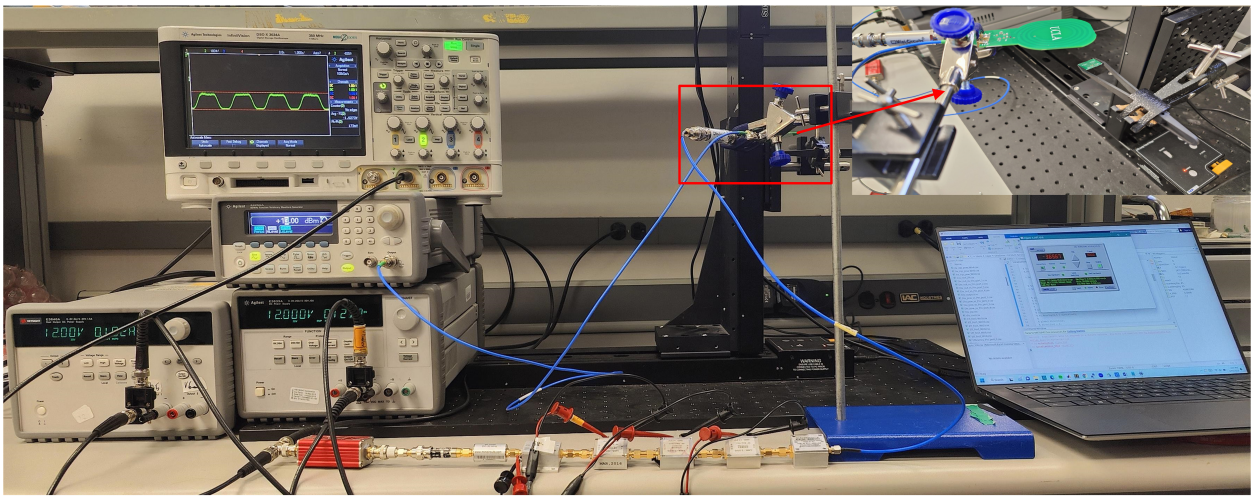

(b)

Figure 3.18: (a) Schematic and (b) picture of the measurement setup for sensing the distance moved by the localizer

3.3.3.2 Sensing the distance moved

Another measurement setup, as illustrated by Fig. 3.18 (a), is used to sense the distance moved by the localizer. Fig. 3.18 (b) shows the picture of the setup. The power of the received signal is also used to modulate the 40.68 MHz TX power signal, causing savings

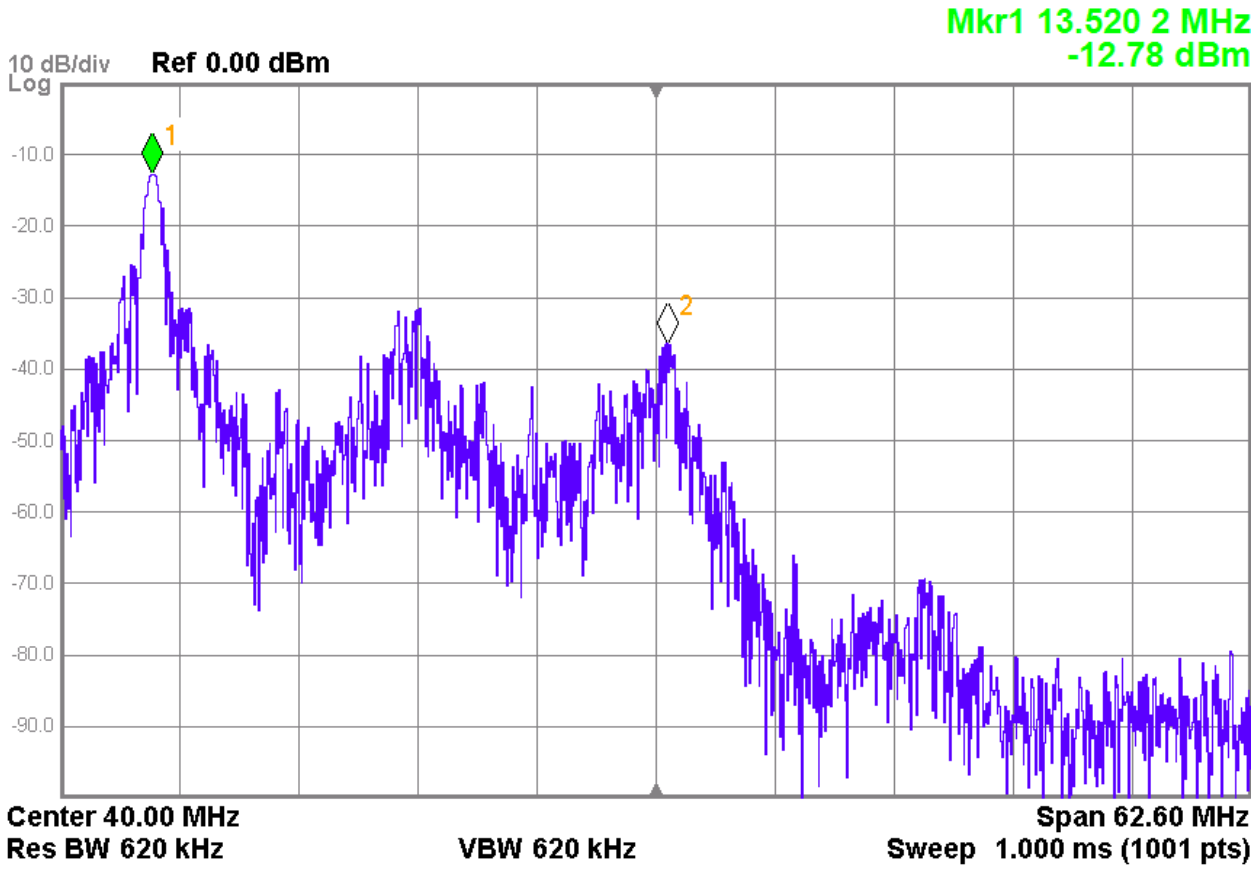

Figure 3.19: Spectrum of the signal at the input of the power detector after it is attenuated by 30 dB. Isolation of more than -20 dB is achieved between the received 13.56 MHz tone and the coupled 40.68 MHz tone

in TX power. This improves the link efficiency for wireless powering while maintaining a minimum SNR for the received signal. For this measurement, a double-tuned double-input coil, the details of which are given in [42], is used. The double-tuned coil is matched to the frequencies of 40.68 MHz (HF) and 13.56 MHz (LF) at the HF and LF inputs, respectively. It has a matching of -26.2 dB and -21.5 dB at HF and LF, respectively, and an isolation of -17.7 dB and -11.7 dB at each port. This coil acts as both the TX and RX coil and has been shown to reduce inter-coil couplings compared to a two-coil system (separate TX and RX coils). The localizer is placed at a distance of 10 mm from the double-tuned coil and

is periodically moved up and down in the Z-direction by distances ranging from 50 to 1000 μm using a motorized rail (Thorlabs LTS300). A 40.68 MHz RF signal of 13 dBm power is delivered to the double-tuned coil for wireless powering. Although a larger operating range can be obtained using a higher TX power, it significantly increases the coupling of the 40.68 MHz signal to the output, requiring more aggressive filtering to reject this coupled signal. It is important to note that the cascade of filters to reject the coupled 40.68 MHz signal is optional and has been used only to ensure that the received 13.56 MHz signal is visible in the time domain using an oscilloscope. The motion detection measurements can be performed using just the spectrum analyzer to record a spectrogram of the received signal in the time domain.

Since the power of the received 13.56 MHz signal at the LF input is needed to generate the modulation input for the 40.68 MHz RF source, it is filtered out, and the 40.68 MHz coupled signal is rejected using the cascade of a low-pass filter (LPF) having a cut-off frequency of 22 MHz (Mini-Circuits BLP-21.4+) and a band-pass filter (BPF) having a passband between 12 and 15 MHz (Mini-Circuits ZFBP-13.5S+). The signal obtained after filtering is passed through a chain of low-noise amplifiers (RF Bay LNA-1050, RF Bay LNA-1800, and RF Bay LNA-500H), providing a total gain of 100 dB. The resultant signal is then passed through a 6 dB splitter (Mini-Circuits ZFRSC-42-S+), and one of the branches is connected to a 30 dB attenuator followed by the spectrum analyzer (Keysight PXA N9030A). The other branch is used for detecting the power of the amplified and filtered signal using a power detector (HP 8473C). The power detector output is passed through an LPF with a cut-off frequency of 5 kHz (Thorlabs EF114) and sent to the oscilloscope for sensing. Fig. 3.19 shows the spectrum of the signal at the input of the power detector, while Fig. 3.20 (a)-(e) shows the oscilloscope waveforms obtained when the localizers are moved by a distance of 50, 100, 200, 500 and 1000 μm respectively. Fig. 3.20 (f) shows the peak-to-peak voltage obtained at the oscilloscope with respect to the distance moved.

The oscilloscope input is then also connected to the modulation input of the RF signal

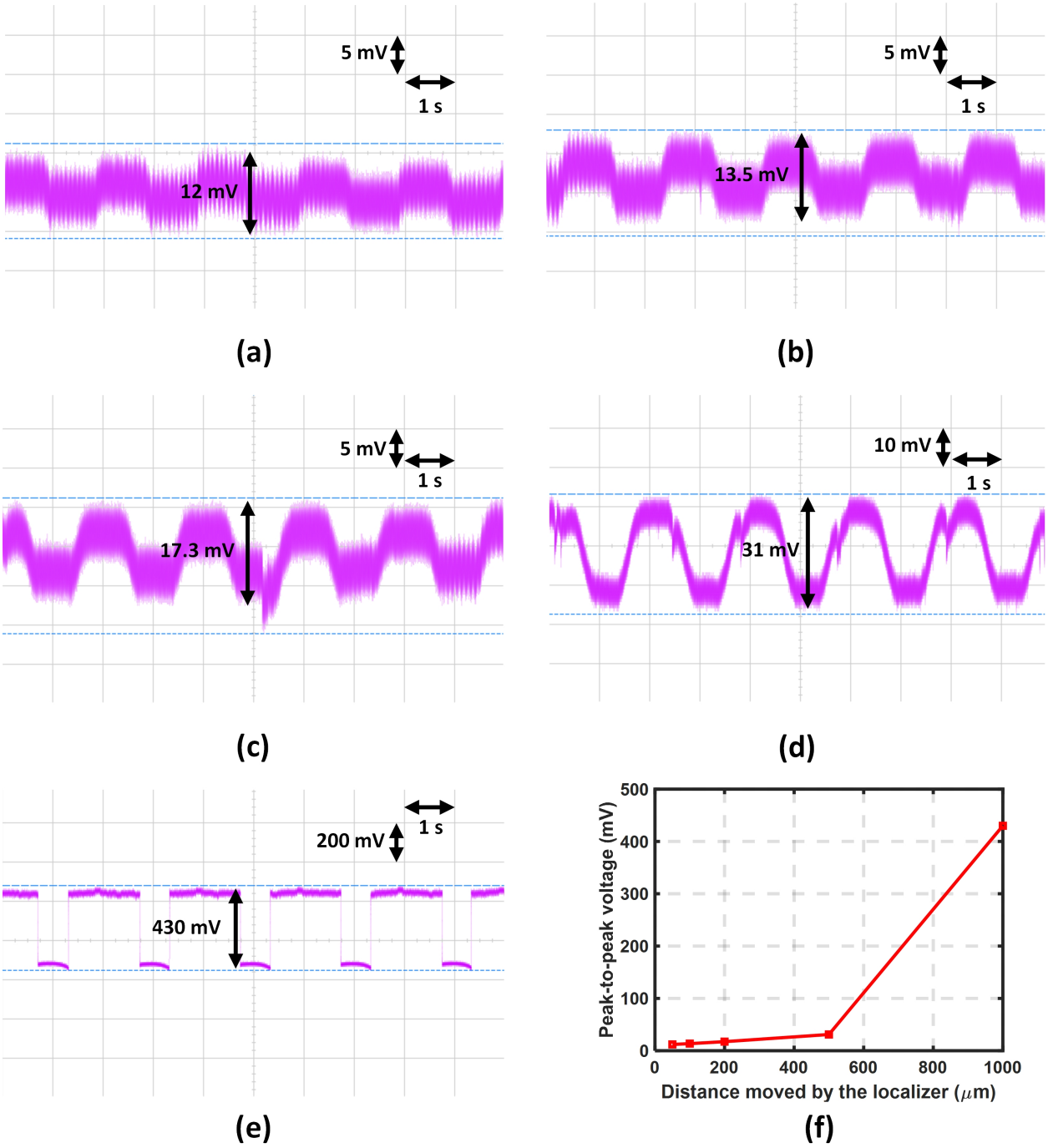

Figure 3.20: Oscilloscope waveforms obtained when the localizer moves by (a) 50 (b) 100 (c) 200 (d) 500 and (e) 1000 μm (f) Peak-to-peak voltage versus distance moved by the localizer

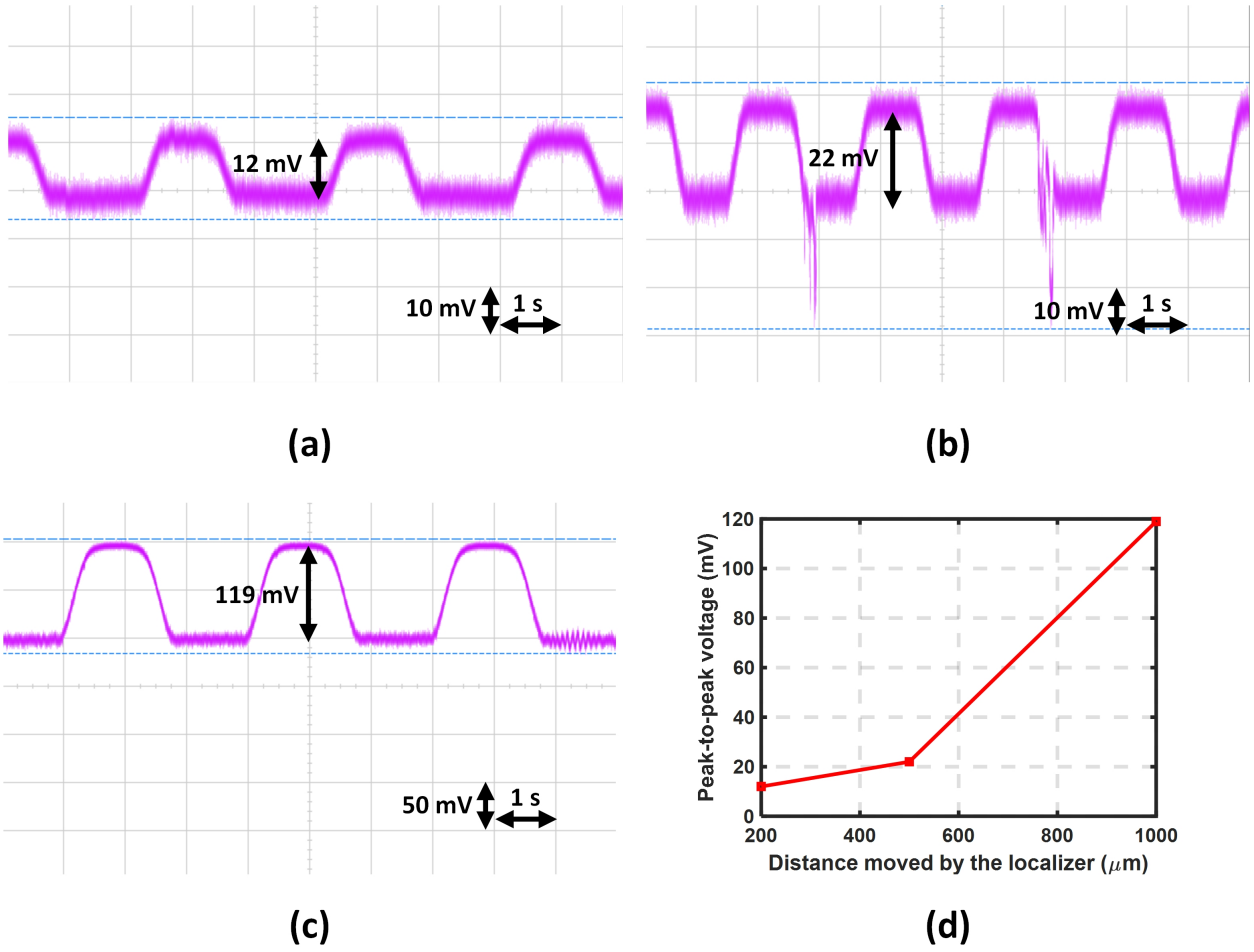

Figure 3.21: Oscilloscope waveforms obtained when the oscilloscope input is connected to the modulation input of the RF source, and the localizer moves by (a) 200 (b) 500 and (c) 1000 μm (d) Peak-to-peak voltage versus distance moved by the localizer in this case

source that generates the 40.68 MHz TX signal. When the localizer is closer to the double-tuned coil, an increase in the power detected leads to a more negative DC voltage generated at its output. When this voltage is fed back to the RF source, it reduces the power of the 40.68 MHz TX signal. Similarly, when the localizer is farther away, a decrease in the power detected increases the power of the 40.68 MHz TX signal. Therefore, this leads to savings in TX power. The modulation index of the RF signal source determines the savings in TX power. At a modulation index of 100%, the TX power can be reduced by a maximum of 3

dB. Fig. 3.21 (a)-(c) shows the oscilloscope waveforms obtained when the oscilloscope input is connected to the modulation input of the RF source, and the localizers are moved by a distance of 200, 500, and 1000 μm respectively. Fig. 3.21 (d) shows the peak-to-peak voltage obtained at the oscilloscope with respect to the distance moved.

Table 3.2 compares the performance of this system with previous localization systems.

3.4 Conclusion

A fully battery-less wirelessly powered localization system with an ultra-low average power consumption of 6 μW has been presented in this chapter. The low power consumption of the IC, fabricated in 0.18 μm technology, is due to the sub-harmonic locking scheme, which uses the RF power signal to generate the signal transmitted by the localizer. This enables it to be reliably powered wirelessly at a distance of 40 mm with a minimum TX power of 2 W. The localization system has an error of less than 5 mm, and this has been verified ex vivo using a porcine intestine. Moreover, it has also been verified to detect a motion as small as 50 μm, as well as rates of motion up to 10 beats per minute. The received signal for this system has also been used to control the power of the transmitter adaptively, leading to further savings in the TX power of the system. Due to its extremely small form factor of 17 mm $\times$ 12 mm $\times$ 0.2 mm, the localizer can be fabricated on a flexible polyimide substrate, enabling it to be used inside 000-sized capsules for next-generation WCE and other biomedical sensor network applications.

Table 3.2: Performance Comparison with Previous Localization Systems

	This work	Nat. Ele. '23 [43]	SSC-L '23 [44]	JSSC '18 [45]	Nat. Bio. '17 [46]
Technology (μm)	**0.18**	N/A*	0.18	0.18	0.18
Wireless power	**Yes**	No	No	No	No
Downlink frequency (MHz)	**40.68**	2400	2.048	40	500
Uplink frequency (MHz)	**13.56**	2400	57	160	480-520
Avg. power (μW)	**6****	180-240	336	9880	339
Excitation power (W)	**2**	60	NM****	N/A*	NM****
Excitation coil size (number)	**3.5 cm diameter (1)**	X, Y : 60 cm × 30 cm ; Z : 60 cm dia. (1)	10 cm × 10 cm (6)	N/A*	0.5 cm diameter (1)
Localization dimension	**2D**	3D	3D	2D	2D
Localization modality	**RF with inductive magnetic coupling**	Magnetic gradient; spatial encoding	Inductive magnetic field	RF	Magnetic gradient; frequency encoding
Accuracy (mm)	**< 5*****	<7.5	<1	<10	<1
Measurement latency (ms)	**11.3**	300	1000	NM****	5
Motion detection	**Yes**	No	No	No	No
Point-of-care application	**Yes**	Yes	No	Yes	Yes

*N/A: Not Applicable **No wireless data transfer ***Raw data; no data processing ****NM: Not mentioned

CHAPTER 4

A Wirelessly Powered System of Coherent Sensing Nodes for Fracture Mapping Applications at Temperatures Upto 250°C and Pressures Upto 24 MPa

This chapter describes a wirelessly powered system of coherently transmitting sensor nodes having a small form factor, low measurement latency, and ultra-low power consumption. These nodes use the received 40.68 MHz RF signal to transmit back a sub-harmonic 13.56 MHz RF signal, therefore aggressively minimizing power consumption in comparison to the traditionally used transmitting techniques such as oscillators or PLLs. The amplitude of the received signal can be used to detect the location of the node. These nodes are experimentally verified to transmit power coherently, enabling their use in WSNs. The nodes were also used for fracture mapping applications using a prototype in both one and two dimensions. Moreover, these nodes are verified to transmit back power at temperatures up to 250 °C. Therefore, they can be used for fracture mapping at high temperatures in oil and gas fields for applications such as hydraulic fracturing.

4.1 System Details

The proposed system for fracture mapping includes several printed circuit boards (PCBs) fabricated on FR4 or flexible polyimide substrates acting as nodes for receiving and transmitting RF signals. These PCBs are hereafter referred to as localizers in the rest of the article. Fig. 4.1 illustrates the localizer and annotates its dimensions. Each localizer con-

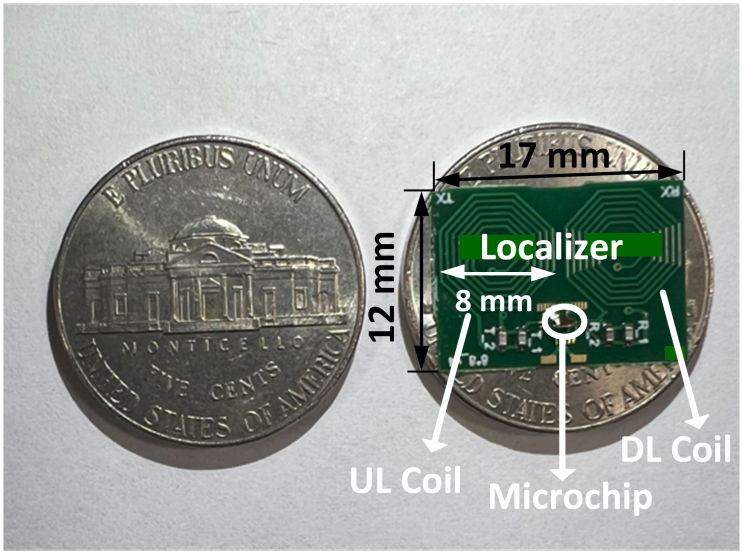

Figure 4.1: Localizer image with size compared to a nickel

sists of a microchip and two identical coils. The RF power transmitted by the TX coil is received by the on-PCB downlink (DL) coil, while the RF power is transmitted from the microchip using the on-PCB uplink (UL) coil, which is received by the RX coil. Capacitors of values 16.8 pF and 160 pF are connected in parallel to the DL and UL coils respectively. This causes the DL and UL coils to resonate at 40.68 MHz and 13.56 MHz, respectively, improving the received and transmitted power at these desired frequencies. The design of the wireless power transfer link has already been described in Chapter 2, therefore, this chapter describes the rest of the system.

The microchip includes a full-wave rectifier, a diode limiter, and a digital divide-by-3 circuit with buffers. The block diagram of the localizer, including the microchip, is shown in Fig. 4.2. A passive 1-stage cross-coupled topology is chosen for the rectifier, as shown in Fig. 4.3. Cross-coupled rectifiers have been shown to have higher power conversion efficiency (PCE) than other topologies [39, 40], improving the link efficiency of the system. Coupling capacitors of 6 pF are used for the rectifier to pass the differential input signal with less than 1% attenuation. The transistors are sized to have maximum efficiency. A 1.8 nF on-chip storage capacitor (C_p) is used to reduce the ripple at the output of the rectifier. The diode

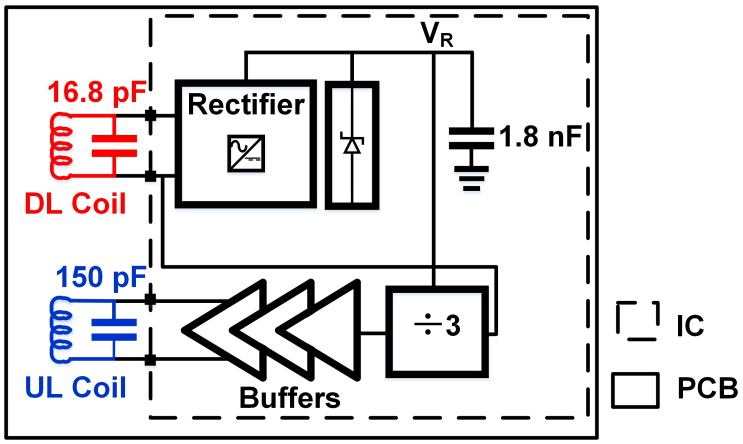

Figure 4.2: Localizer architecture

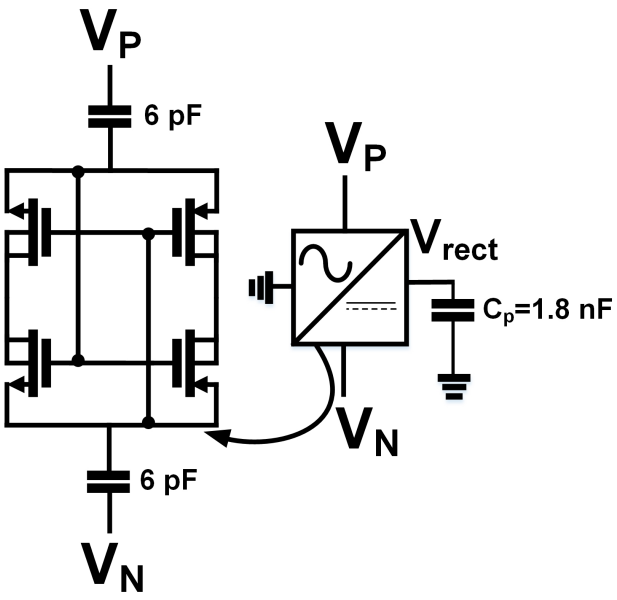

Figure 4.3: Rectifier schematic

limiter limits the output voltage of the rectifier to 3.8 V, providing over-voltage protection to the microchip. The output voltage of the rectifier V_R works as a supply voltage for the digital divide-by-3 circuit, which divides the frequency of the received RF power signal by 3. The divide-by-3 circuit, as illustrated in 3.8(a), includes a mod-3 counter and D flip-flops with an asynchronous set-reset operation. The divide-by-3 ensures sub-harmonic locking of

the frequency of the received RF signal to that of the transmitted signal. The divide-by-3 circuit has an extremely low power consumption of 1.5 μW for the lowest amplitude of the RF input signal, for which it generates a measurable output.

Since multiple localizers placed at different locations transmit signals back to the RX coil, it is imperative to synchronize the frequency and phase of the signals received from different localizers so that they can constructively add up at the RX. Conventionally, this has been done using oscillators in phase-locked loops (PLLs) as transmitters [13]. However, PLLs have the drawbacks of using an off-chip crystal oscillator for precise reference frequency generation. Moreover, PLLs are extremely power-hungry and, therefore, unsuitable for wireless powering applications. Another feasible way to do this is by using injection-locked power oscillators as transmitters [14–16]. However, these oscillators consume static power and have a limited locking range which decreases with an increase in the quality factor of inductors, requiring a higher amplitude of injection RF signal for certain applications. For our application, the phase differences between different localizers can be neglected since the operating range is lesser than the wavelength at the operating frequency by at least an order of magnitude. The divide-by-3 circuit does not consume static power and does not require the generation of an injection RF signal. Moreover, the frequency of the transmitted signal is always locked to the frequency of the received signal, enabling the use of the entire bandwidth allowed by the ISM band.

The PCE of the rectifier and the peak-to-peak values of the divider output are simulated. Fig. 4.4 shows the (a) PCE of the rectifier and (b) peak-to-peak divider output voltage versus input power for 1, 2, 3, and 4- stage rectifiers. Reducing the sensitivity and increasing the transmitted power is paramount for increasing the operating range of the system. The sensitivity of the system is determined by that of the rectifier and the divider. The sensitivity of the rectifier is defined as the minimum input power for which it generates a supply voltage that is large enough for the divider. The sensitivity of the divider, on the other hand, is defined as the minimum input power for which it generates a detectable peak-to-peak output.

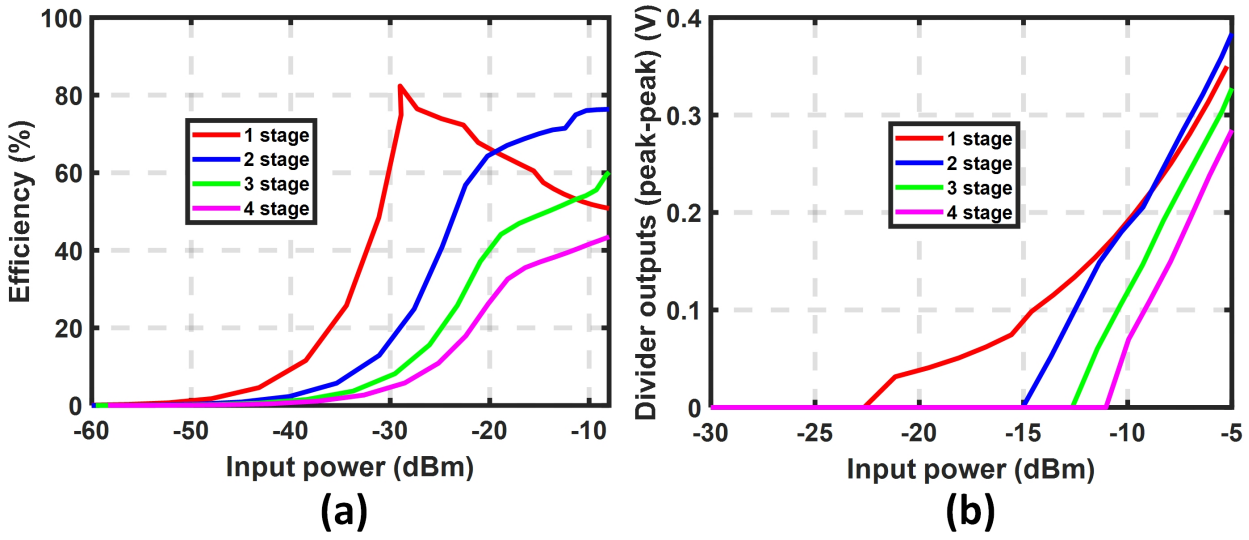

Figure 4.4: Simulated (a) Rectifier efficiency and (b) peak-to-peak divider output voltage versus input power for 1, 2, 3, and 4-stage rectifiers. 1-stage rectifier shows the best sensitivity for both rectifier and divider

From Fig. 4.4, it is observed that reducing the number of stages in the rectifier increases the sensitivity of both the rectifier and the divider. Increasing the number of stages generates a larger supply voltage, and therefore, more transmitted power but reduces the sensitivity. Since a much larger RF power is required to power the microchip than detect the transmitted power, sensitivity dominates over transmitted power. Therefore, only one stage is used for the rectifier.

4.2 Measurement Results

The annotated die micrograph of the microchip having dimensions of 1.1 mm X 0.56 mm is shown in Fig. 4.5. The microchip was fabricated using TSMC 0.18 μm process. A signal generator (HP 8340B) generates the RF signal used for powering the microchips. The RF power of the signal was increased by connecting the output of the signal generator to a power amplifier (PA) (Minicircuits ZHL-20W-13+) having a small signal gain of 50 dB and

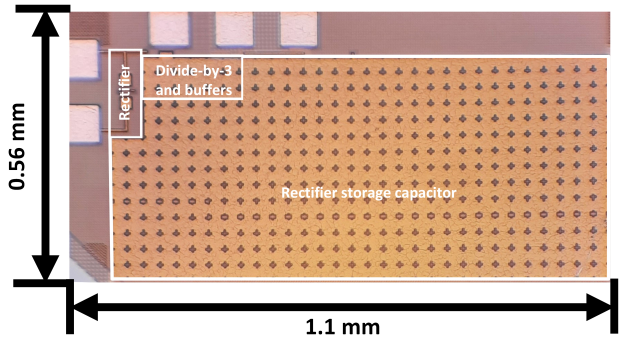

Figure 4.5: Die micrograph

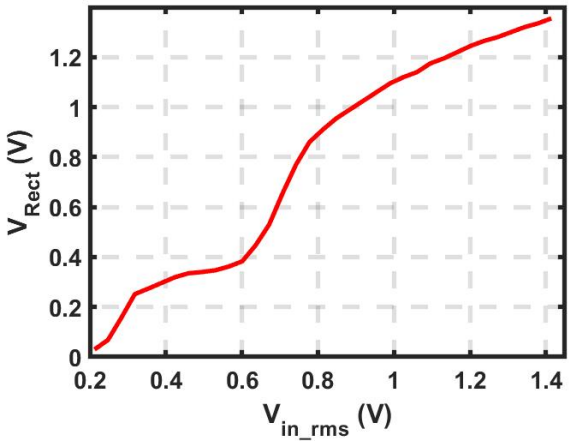

Figure 4.6: Measured rectifier voltage with respect to input rms voltage

a saturated output power of 20 W, increasing the operating range of the system. A spectrum analyzer (Tektronix RSA 306B) is used to measure the magnitude of the received RF signal. The following subsections report all the measurements performed using the localizers.

4.2.1 Energy harvesting verification

For this measurement, the input terminals of the rectifier are wired to the RF signal generator to generate an RF signal at 40.68 MHz, and the DC output of the rectifier is measured using an oscilloscope. Fig. 4.6 shows the rectifier output voltages for different root mean square (rms) input voltages. It is observed that the rectifier generates sufficient DC voltage to power

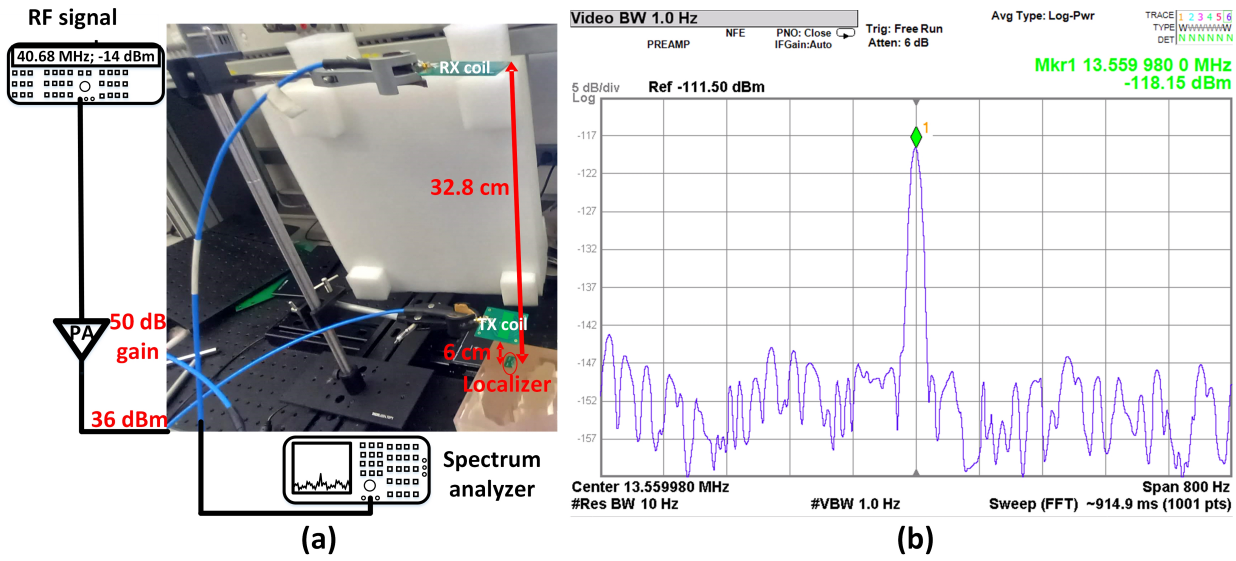

Figure 4.7: (a) Measurement setup used for chip functionality verification; (b) Received signal spectrum at the maximum operating range

the microchip at input rms voltages above 0.8 V.

4.2.2 Microchip functionality verification

The measurement setup used for verifying the functionality of the microchip is illustrated in Fig. 4.7 (a). The maximum operating range of the system is determined using the largest amplitude of RF signal available in the laboratory. Using the RF signal generator, a 40.68 MHz RF signal with -14 dBm power is delivered to the power amplifier with a small signal gain of 50 dB. Therefore, an RF power of 36 dBm is delivered to the TX coil. The RX coil is connected to the spectrum analyzer for detecting the received power from the localizer. Keeping the RX coil very close to the localizer, the distance between the localizer and the TX coil is increased until the received 13.56 MHz tone merges with the noise floor of the spectrum analyzer. It is observed that the localizer can be wirelessly powered at a maximum distance of 6 cm between the localizer and the TX coil with 36 dBm power. Increasing the TX power would increase this maximum distance. Keeping the distance between the

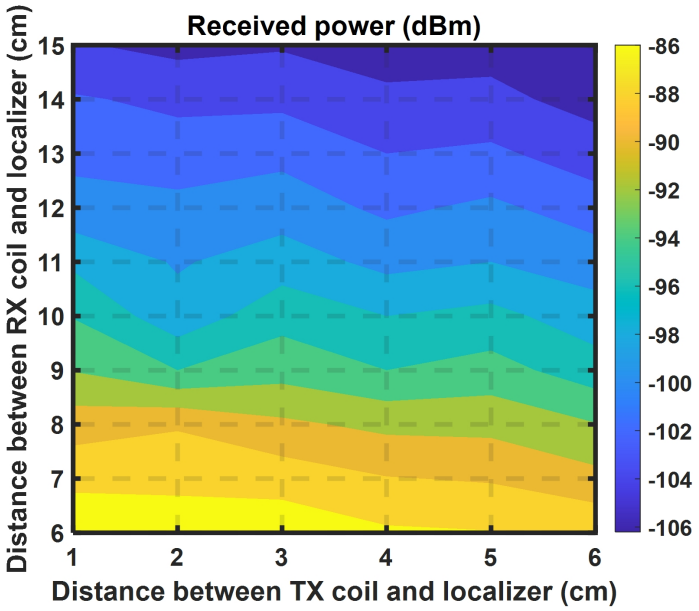

Figure 4.8: Received 13.56 MHz signal power in dBm across different separations between the TX coil and the localizer DL coil, and the RX coil and the localizer UL coil

localizer and the TX coil fixed at 6 cm, the distance between the localizer and the RX coil is then increased till the received 13.56 MHz tone merges with the noise floor of the spectrum analyzer. It is observed that the RF signal transmitted from the localizer can be received by the RX coil at a maximum distance of 32.8 cm from it. While performing this measurement, since the received signal frequency was locked to that of the transmitted signal, the span and resolution bandwidth of the spectrum analyzer could be reduced, helping in lowering its noise floor. Fig. 4.7(b) shows the received 13.56 MHz tone having -118.15 dBm power at 6cm and 32.8 cm distance between the localizer and TX and RX coil, respectively.

Using the same setup, the received power is recorded for different separations between (a) the TX coil and the localizer DL coil and (b) the RX coil and the localizer UL coil. For each separation distance between the TX coil and the localizer DL coil, the lowest TX power required to power the microchip is used to maintain uniformity in the received power for different distances. Fig. 4.8 illustrates the contour plot of the received power profiles across different separations.

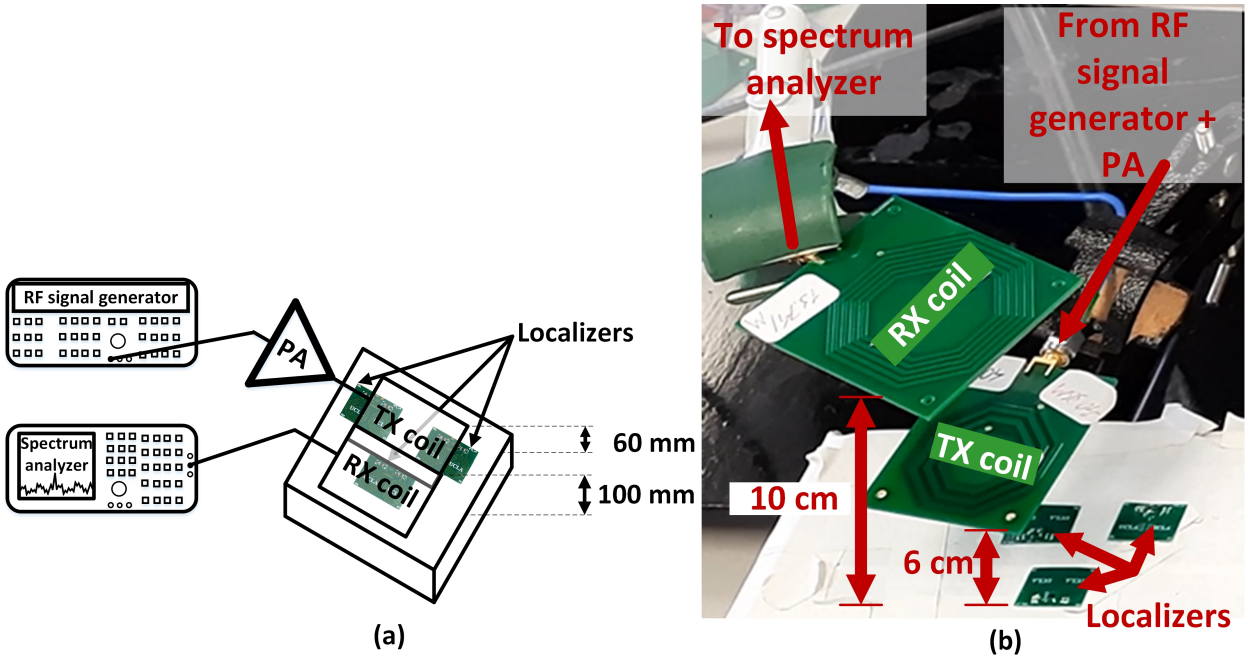

Figure 4.9: (a) Schematic and (b) picture of the coherent power combining setup

4.2.3 Coherent power combining verification

The measurement setup used for verifying the coherent power combining of RF signals transmitted by different localizers is illustrated in Fig. 4.9. A 40.68 MHz TX power signal of -14 dBm is amplified to 36 dBm using the PA as in the previous measurement. In three different measurements, one, two, and three localizers are placed close to each other on a surface such that they can be wirelessly powered by the same TX coil. The TX and RX coils are placed at a distance of 6 cm and 10 cm, respectively, from the localizers to transmit and receive RF signals from them. A spectrum analyzer (Tektronix RSA 306B) is connected to the RX coil to measure the power received from the localizers. Fig. 4.10 shows the power received at 13.56 MHz from (a) one, (b) two, and (c) three localizers. It is observed that the power received from two and three localizers (around 2 pW and 3 pW, respectively) is almost equal to twice and thrice that received from one localizer (around 1 pW), which verifies the fact that the signals transmitted by the localizers add up coherently.

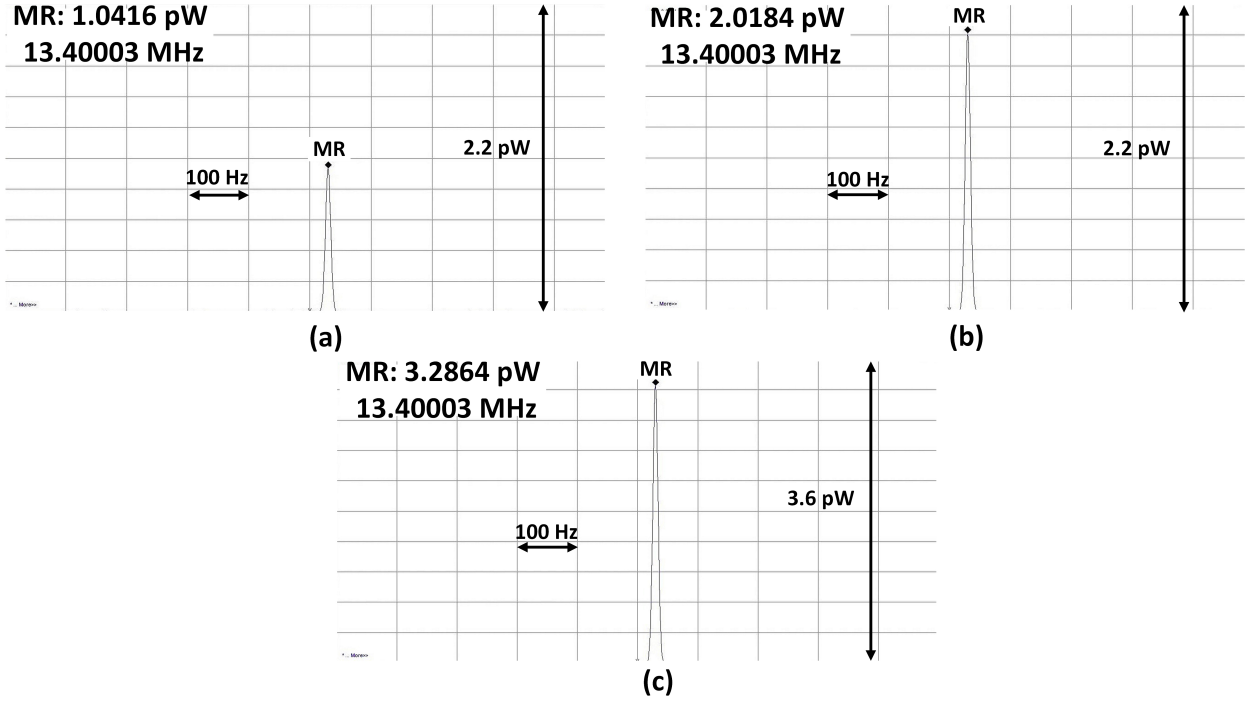

Figure 4.10: Received power from (a) one, (b) two, and (c) three localizers

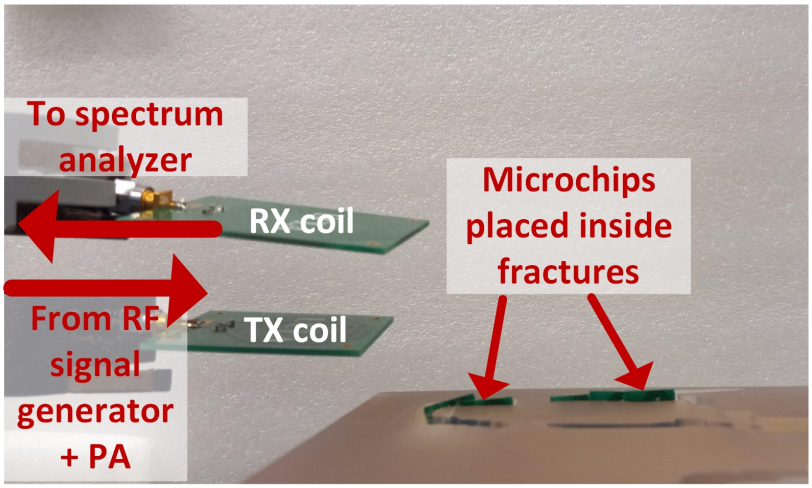

Figure 4.11: Fracture mapping setup

4.2.4 Fracture mapping verification

The measurement setup used for fracture mapping measurements is illustrated in Fig. 4.11. For this measurement, a prototype of a rock with fractures along its height is used to mimic

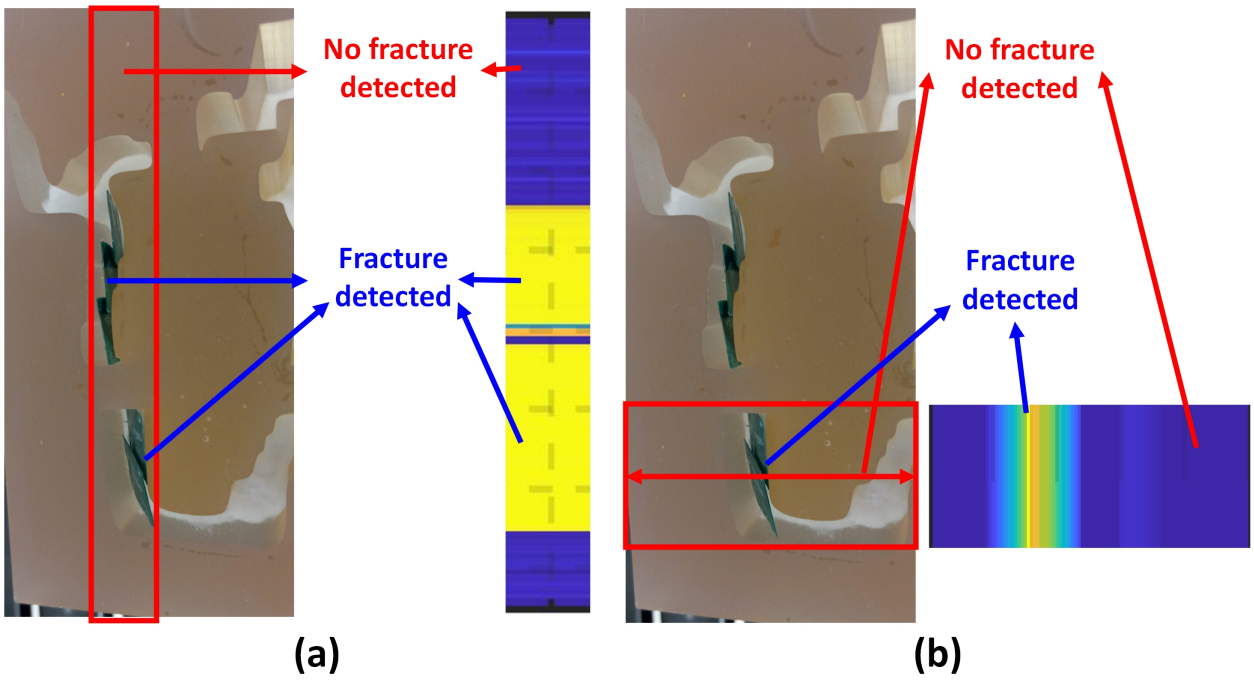

Figure 4.12: 1D fracture mapping results for (a) y-direction and (b) x-direction. The red box indicates the region that was mapped

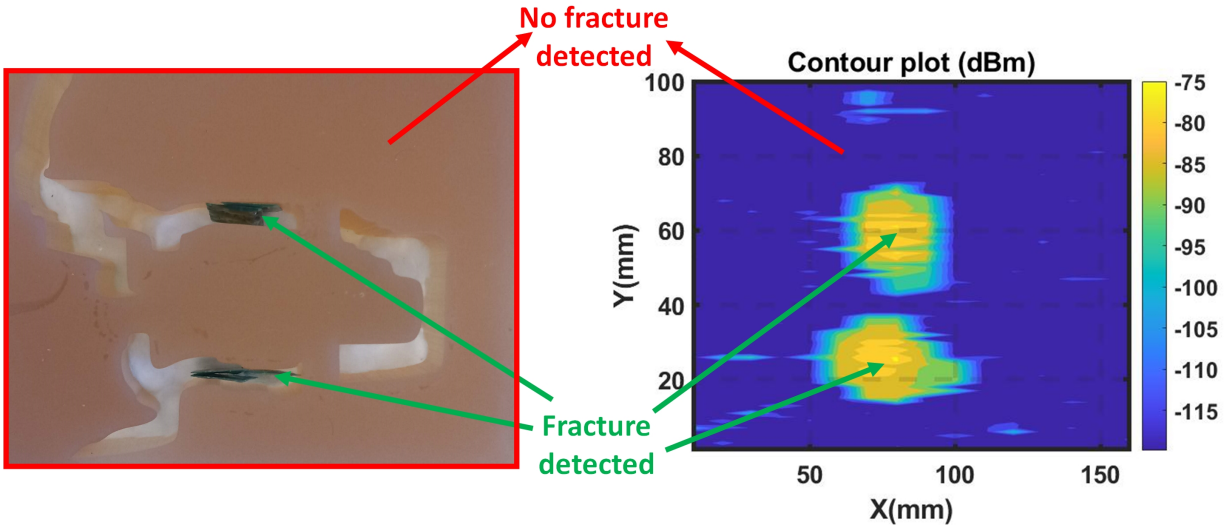

Figure 4.13: 2D fracture mapping results. The red box indicates the region that was mapped

the hydraulic fractures in the oil and gas wells. The localizers are coated with non-conductive epoxy and are placed inside the fractures that are to be mapped. The distances of the TX and RX coils from the fractures are similar to the previous measurements. Using motorized rails in the X and Y directions, the TX and RX coils are moved over the entire region that is desired to be mapped. The presence or absence of a fracture at a specific coordinate is determined by the presence or the absence of a 13.56 MHz tone in the received signal. A spectrum analyzer is connected to the RX coil to record the spectrum at different coordinates, which is, in turn, connected to a laptop for data processing using MATLAB. The fractures are mapped in the X and Y directions separately with a resolution of 1 mm in both X and Y directions. Fig. 4.12(a) illustrates the fracture mapping results for the Y-direction, while 4.12(b) illustrates the same for the X-direction. Fig. 4.13 illustrates the 2D fracture mapping results. It is observed that the fractures are mapped with considerable accuracy using the localizers.

4.2.5 High temperature verification

The functionality of the localizers is also verified at high temperatures. The schematic and picture of the measurement setup for the high-temperature measurements are shown in Fig. 4.14(a) and (b) respectively. In this measurement, the localizer is placed inside a microwave oven. The RF signal generator and power amplifier are used to generate a 36 dBm 40.68 MHz power signal as in the previous measurements. It is observed that at the previously measured maximum distance of 6 cm between the TX coil and the localizer, the rectifier does not generate enough DC voltage for the proper functioning of the microchip at higher temperatures. The TX coil is therefore positioned at a distance of 2 cm from the localizer inside the oven so that the microchip can be powered at all temperatures in the range of our measurements. The RX coil is connected to the spectrum analyzer and placed at a distance of 10 cm from the localizer. The temperature inside the oven is increased using the knob on the oven. The oven temperature is measured by an oven thermometer (Admetior

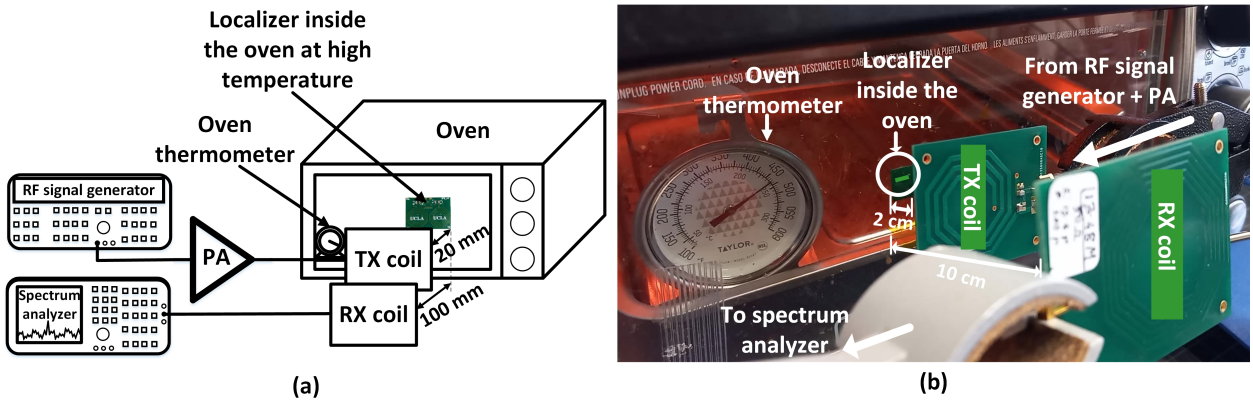

Figure 4.14: (a) Schematic and (b) picture of the measurement setup for verification at high temperatures

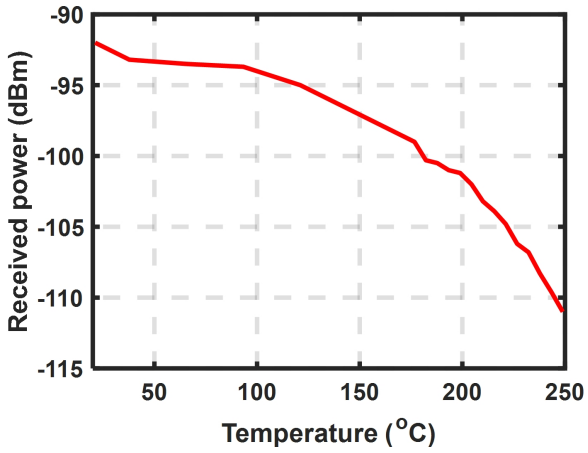

Figure 4.15: Received signal power at temperatures from 20 - 250°C

Kitchen Oven Thermometer). Fig. 4.15 shows the received signal power from the localizer at temperatures from 20 to 250 °C.

4.2.6 High pressure verification

The localizers are also verified to work under high-pressure conditions using a concrete compression sensing machine. Wet cement is placed inside three different cube-shaped molds

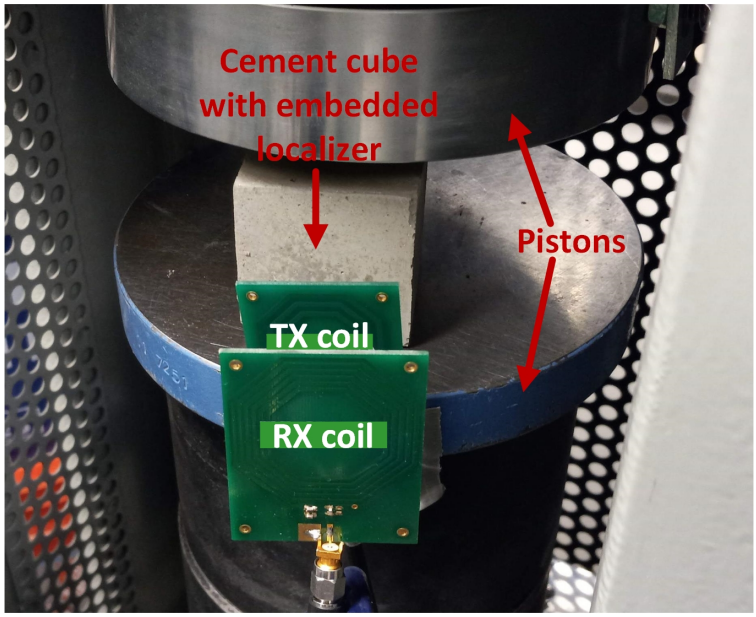

Figure 4.16: Measurement setup for verification at high pressures. The entire setup is inside a compression sensing machine.

and allowed to cure for 24 hours. While pouring the wet cement into the molds, one localizer is placed in each mold at a depth of 1 cm from the bottom. Each cube with a localizer embedded in it is then placed in the compression sensing machine, and a compressive force is applied using the cylindrical pistons from the top and bottom. The high-pressure measurement setup is illustrated in Fig. 4.16. The RF signal generator and power amplifier are used to generate a 36 dBm 40.68 MHz power signal as in the previous measurements. Due to the metallic nature of the compression sensing machine, the distance of the TX and RX coils from the localizer is reduced such that the localizer can be powered. The applied compressive pressure is slowly increased till the cement cubes fracture. The three cubes fracture at pressures of 8.53 MPa (1237 psi), 24.06 MPa (3490 psi), and 18.40 MPa (2669 psi), respectively. Fig. 4.17 (a) shows the second cube after it fractures. The received 13.56 MHz tone from the localizer is still observed even at the highest of these pressures (3490 psi). Fig. 4.17 (b) shows the received signal from the second localizer when the second cube fractures at 24 MPa pressure.

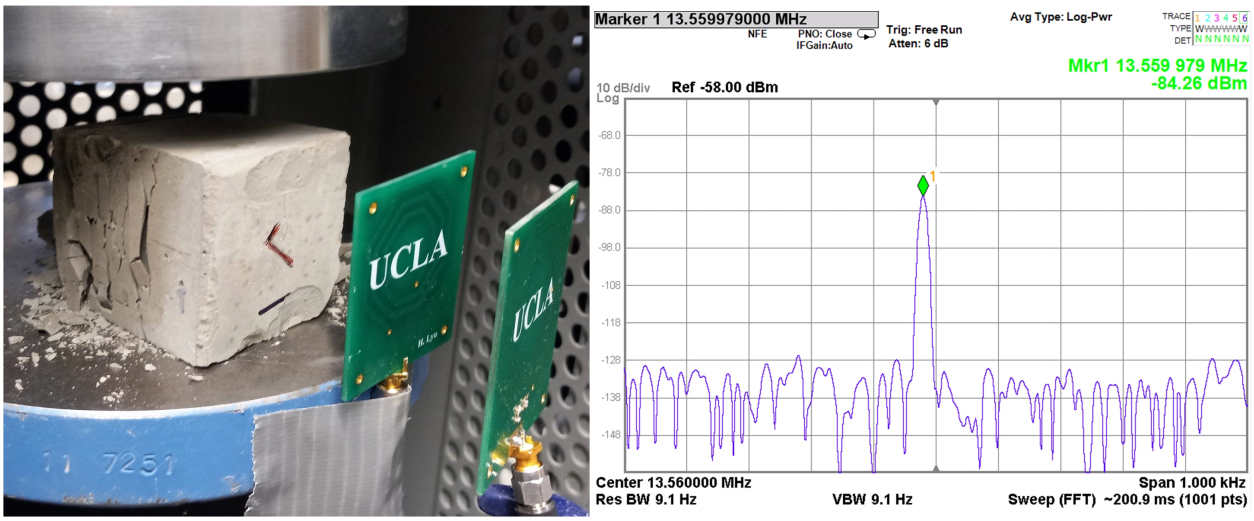

Figure 4.17: (a) The second cube after it fractures at 24 MPa; (b) Received signal from the second localizer when the second cube fractures.

4.3 Conclusion

In this paper, a wirelessly powered system of coherent sensing nodes has been presented and proposed for use in fracture mapping applications at high temperatures. A power-efficient scheme using the RF power signal and a digital divide-by-3 circuit has been used to generate a locked sub-harmonic signal to be transmitted by the microchip. This enables an average power consumption of only 1.5 μW for the system. The system has also been verified to work reliably at temperatures up to 250 °C and pressures up to 24 MPa, which are one of the highest using a standard CMOS process. The system, having a small form factor and ultra-low power consumption, also finds use in other sensing and localization applications using WSNs.

CHAPTER 5

Summary and Future Directions

In this thesis, two miniaturized wireless and battery-less localization systems are presented and proposed for use in WSNs. The first system was used for performing two-dimensional localization and motion sensing. With a measurement latency of 11.3 ms and an accuracy of less than 5 mm, the system offers fast and accurate scanning capabilities desirable for biomedical localization applications. In vitro and ex vivo measurement results using this system inside the porcine intestine are also presented in the thesis. The second system was used for mapping fractures at temperatures up to 250 °C and pressures up to 24 MPa. The techniques used for wireless power transfer link modeling and the design of the near-field coupling coils for implementing the link are also analyzed in this thesis.

In future iterations of the localization system not included in this thesis, efforts have been made to reduce the form factor of the localizer to 8 mm $\times$ 10 mm by increasing the number of layers in the PCB and laying out the TX coil and RX coil at the same location in different layers. This inadvertently increases the coupling between the two coils, therefore careful simulations were performed to determine the PCB thickness to ensure the link performance. The use of SMD inductors for wireless power transfer has also been investigated.

Future directions of this work could involve improving link efficiency by using a transmitter to generate a stronger tone at the output. The system could also include a transceiver and be used for data communication, therefore incorporating biomedical signal sensing and localization on the same chip. The localization system can be packaged and used inside capsules for wireless capsule endoscopy applications.

REFERENCES

[1] D. Kandris, C. Nakas, D. Vomvas, and G. Koulouras, "Applications of wireless sensor networks: an up-to-date survey," *Applied system innovation*, vol. 3, no. 1, p. 14, 2020.

[2] H. Landaluce, L. Arjona, A. Perallos, F. Falcone, I. Angulo, and F. Muralter, "A review of iot sensing applications and challenges using rfid and wireless sensor networks," *Sensors*, vol. 20, no. 9, p. 2495, 2020.

[3] I. F. Akyildiz, W. Su, Y. Sankarasubramaniam, and E. Cayirci, "Wireless sensor networks: a survey," *Computer networks*, vol. 38, no. 4, pp. 393–422, 2002.

[4] S. R. Islam, D. Kwak, M. H. Kabir, M. Hossain, and K.-S. Kwak, "The internet of things for health care: a comprehensive survey," *IEEE access*, vol. 3, pp. 678–708, 2015.

[5] S. Amendola, R. Lodato, S. Manzari, C. Occhiuzzi, and G. Marrocco, "Rfid technology for iot-based personal healthcare in smart spaces," *IEEE Internet of things journal*, vol. 1, no. 2, pp. 144–152, 2014.

[6] D. Sarikaya, J. J. Corso, and K. A. Guru, "Detection and localization of robotic tools in robot-assisted surgery videos using deep neural networks for region proposal and detection," *IEEE transactions on medical imaging*, vol. 36, no. 7, pp. 1542–1549, 2017.

[7] I. Vlachos, B. Krishnan, D. M. Treiman, K. Tsakalis, D. Kugiumtzis, and L. D. Iasemidis, "The concept of effective inflow: application to interictal localization of the epileptogenic focus from ieeg," *IEEE Transactions on Biomedical Engineering*, vol. 64, no. 9, pp. 2241–2252, 2016.

[8] R. Jin and B. Jung, "Magnetic tracking system for heart surgery," *IEEE Transactions on Biomedical Circuits and Systems*, vol. 16, no. 2, pp. 275–286, 2022.

[9] T. D. Than, G. Alici, H. Zhou, and W. Li, "A review of localization systems for robotic endoscopic capsules," *IEEE transactions on biomedical engineering*, vol. 59, no. 9, pp. 2387–2399, 2012.

[10] H. Mateen, R. Basar, A. U. Ahmed, and M. Y. Ahmad, "Localization of wireless capsule endoscope: A systematic review," *IEEE Sensors Journal*, vol. 17, no. 5, pp. 1197–1206, 2017.

[11] G. L. Barbruni, P. M. Ros, D. Demarchi, S. Carrara, and D. Ghezzi, "Miniaturised wireless power transfer systems for neurostimulation: A review," *IEEE Transactions on Biomedical Circuits and Systems*, vol. 14, no. 6, pp. 1160–1178, 2020.

[12] A. Costanzo and D. Masotti, "Energizing 5g: Near-and far-field wireless energy and data trantransfer as an enabling technology for the 5g iot," *IEEE Microwave Magazine*, vol. 18, no. 3, pp. 125–136, 2017.

[13] B. Razavi, "The role of plls in future wireline transmitters," *IEEE Transactions on Circuits and Systems I: Regular Papers*, vol. 56, no. 8, pp. 1786–1793, 2009.

[14] Y. Sun and A. Babakhani, "A wirelessly powered injection-locked oscillator with on-chip antennas in 180-nm soi cmos for spectroscopy application," *IEEE Sensors Letters*, vol. 3, no. 7, pp. 1–4, 2019.

[15] B. Jamali and A. Babakhani, "Wireless time transfer with subpicosecond accuracy based on a fully integrated injection-locked picosecond pulse detector," *IEEE Transactions on Microwave Theory and Techniques*, vol. 68, no. 1, pp. 160–169, 2019.

[16] H. Rahmani, Y. Sun, M. Kherwa, S. Pal, and A. Babakhani, "Coherent radiation from a swarm of wirelessly powered and synchronized sensor nodes," *IEEE Sensors Journal*, vol. 20, no. 19, pp. 11608–11616, 2020.

[17] P. A. Charlez, *Rock Mechanics. Volume 2. Petroleum Applications.* Editions Technip, Paris, 1997.

[18] G. W. P. C. (US), A. C. (Firm), U. S. D. of Energy. Office of Fossil Energy, and N. E. T. L. (US), *Modern shale gas development in the United States: A Primer.* US Department of Energy, Office of Fossil Energy, 2009.

[19] D. J. C. Reis, *Environmental control in petroleum engineering.* Elsevier, 1996.

[20] J. H. Le Calvez, R. Klem, L. Bennett, A. Erwemi, M. Craven, and J. Palacio, "Real-time microseismic monitoring of hydraulic fracture treatment: a tool to improve completion and reservoir management," in *SPE Hydraulic Fracturing Technology Conference and Exhibition*, pp. SPE–106159, SPE, 2007.

[21] M. C. Fehler, "Stress control of seismicity patterns observed during hydraulic fracturing experiments at the fenton hill hot dry rock geothermal energy site, new mexico," in *International Journal of Rock Mechanics and Mining Sciences & Geomechanics Abstracts*, vol. 26, pp. 211–219, Elsevier, 1989.

[22] N. Yekeen, E. Padmanabhan, A. K. Idris, and P. S. Chauhan, "Nanoparticles applications for hydraulic fracturing of unconventional reservoirs: A comprehensive review of recent advances and prospects," *Journal of Petroleum Science and Engineering*, vol. 178, pp. 41–73, 2019.

[23] A. Aderibigbe, K. Cheng, Z. Heidari, J. Killough, T. Fuss, and W. T. Stephens, "Detection of propping agents in fractures using magnetic susceptibility measurements enhanced by magnetic nanoparticles," in *SPE Annual Technical Conference and Exhibition*, OnePetro, 2014.

[24] A. Aderibigbe, K. Cheng, Z. Heidari, J. Killough, and T. Fuss-Dezelic, "Application of magnetic nanoparticles mixed with propping agents in enhancing near-wellbore fracture detection," *Journal of Petroleum Science and Engineering*, vol. 141, pp. 133–143, 2016.

[25] T. Sun, *Study on Preparation and performance of nano-ferrofluids used in diagnosticof hydraulic fracture*. PhD thesis, MS thesis, China University of Petroleum (East China), 2016.

[26] J. Liu, S. Cao, X. Wu, and J. Yao, "Detecting the propped fracture by injection of magnetic proppant during fracturing," *Geophysics*, vol. 84, no. 3, pp. JM1–JM14, 2019.

[27] A. A. Alshehri, C. H. Martins, S.-C. Lin, I. F. Akyildiz, and H. K. Schmidt, "Fracbot technology for mapping hydraulic fractures," *SPE Journal*, vol. 26, no. 02, pp. 610–626, 2021.

[28] W. Kumari, P. Ranjith, M. Perera, X. Li, L. Li, B. Chen, B. A. Isaka, and V. De Silva, "Hydraulic fracturing under high temperature and pressure conditions with micro ct applications: Geothermal energy from hot dry rocks," *Fuel*, vol. 230, pp. 138–154, 2018.

[29] P. Dreike, D. Fleetwood, D. King, D. Sprauer, and T. Zipperian, "An overview of high-temperature electronic device technologies and potential applications," *IEEE Transactions on Components, Packaging, and Manufacturing Technology: Part A*, vol. 17, no. 4, pp. 594–609, 1994.

[30] D. Fleetwood, F. Thome, S. Tsao, P. Dressendorfer, V. Dandini, and J. Schwank, "High-temperature silicon-on-insulator electronics for space nuclear power systems: requirements and feasibility," *IEEE Transactions on Nuclear Science*, vol. 35, no. 5, pp. 1099–1112, 1988.

[31] P. G. Neudeck, R. S. Okojie, and L.-Y. Chen, "High-temperature electronics-a role for wide bandgap semiconductors?," *Proceedings of the IEEE*, vol. 90, no. 6, pp. 1065–1076, 2002.

[32] T.-H. Chen, L. T. Clark, and K. E. Holbert, "Memory design for high temperature radiation environments," in *2008 IEEE International Reliability Physics Symposium*, pp. 107–114, IEEE, 2008.

[33] N. Sadeghi, A. Sharif-Bakhtiar, and S. Mirabbasi, "A 0.007-mm^2 108-ppm/°c 1-mhz relaxation oscillator for high-temperature applications up to 180 °c in 0.13 μm cmos," *IEEE Transactions on Circuits and Systems I: Regular Papers*, vol. 60, no. 7, pp. 1692–1701, 2013.

[34] C. Davis and I. Finvers, "A 14-bit high-temperature $\sigma\delta$ modulator in standard cmos," *IEEE Journal of Solid-State Circuits*, vol. 38, no. 6, pp. 976–986, 2003.

[35] A. Ray, I. Habibagahi, and A. Babakhani, "A fully wireless and batteryless localization system with 50 micrometre motion detection capability and adaptive transmitter power control for point-of-care biomedical applications," *IEEE Transactions on Biomedical Circuits and Systems*, 2023.

[36] A. Ray, I. Habibagahi, and A. Babakhani, "Fully wireless and batteryless localization and physiological motion detection system for point-of-care biomedical applications," in *2022 IEEE Biomedical Circuits and Systems Conference (BioCAS)*, pp. 26–30, IEEE, 2022.

[37] A. Ray and A. Babakhani, "A wirelessly powered system of coherent sensing nodes for fracture mapping applications at temperatures upto 250° c and pressures upto 24 mpa," *IEEE Sensors Journal*, 2023.

[38] P. Pérez-Nicoli, F. Silveira, and M. Ghovanloo, *Inductive Links for Wireless Power Transfer*. Springer, 2021.

[39] J. Jang, I. Habibagahi, H. Rahmani, and A. Babakhani, "Wirelessly powered, batteryless closed-loop biopotential recording ic for implantable leadless cardiac monitoring applications," in *2021 IEEE Biomedical Circuits and Systems Conference (BioCAS)*, pp. 1–4, IEEE, 2021.

[40] U. Guler and M. Ghovanloo, "Power management in wireless power-sipping devices: A survey," *IEEE circuits and systems magazine*, vol. 17, no. 4, pp. 64–82, 2017.

[41] B. Razavi, "The low dropout regulator [a circuit for all seasons]," *IEEE Solid-State Circuits Magazine*, vol. 11, no. 2, pp. 8–13, 2019.

[42] I. Habibagahi, R. P. Mathews, A. Ray, and A. Babakhani, "Design and implementation of multisite stimulation system using a double-tuned transmitter coil and miniaturized implants," *IEEE Microwave and Wireless Technology Letters*, vol. 33, no. 3, pp. 351–354, 2022.

[43] S. Sharma, K. B. Ramadi, N. H. Poole, S. S. Srinivasan, K. Ishida, J. Kuosmanen, J. Jenkins, F. Aghlmand, M. B. Swift, M. G. Shapiro, *et al.*, "Location-aware ingestible microdevices for wireless monitoring of gastrointestinal dynamics," *Nature Electronics*, vol. 6, no. 3, pp. 242–256, 2023.

[44] M. Rustom and C. Sideris, "Design and implementation of a low power wireless frequency-division multiplexed magnetic 3d localization scheme with sub-mm precision for capsule endoscopy applications," *IEEE Solid-State Circuits Letters*, vol. 6, pp. 37–40, 2023.

[45] J. Jang, J. Lee, K.-R. Lee, J. Lee, M. Kim, Y. Lee, J. Bae, and H.-J. Yoo, "A four-camera vga-resolution capsule endoscope system with 80-mb/s body channel communication

transceiver and sub-centimeter range capsule localization," *IEEE Journal of Solid-State Circuits*, vol. 54, no. 2, pp. 538–549, 2018.

[46] M. Monge, A. Lee-Gosselin, M. G. Shapiro, and A. Emami, "Localization of microscale devices in vivo using addressable transmitters operated as magnetic spins," *Nature Biomedical Engineering*, vol. 1, no. 9, pp. 736–744, 2017.